Effects of tangential-type boundary condition discontinuities on the accuracy of the lattice Boltzmann method for heat and mass transfer

Like Li,[*] Nick AuYeung,[†] Renwei Mei,[‡] and James F. Klausner[§]
Department of Mechanical and Aerospace Engineering, University of Florida, Gainesville, Florida 32611-6250, USA
(Received 5 September 2014; published 10 August 2016)

We present a systematic study on the effects of tangential-type boundary condition discontinuities on the accuracy of the lattice Boltzmann equation (LBE) method for Dirichlet and Neumann problems in heat and mass transfer modeling. The second-order accurate boundary condition treatments for continuous Dirichlet and Neumann problems are directly implemented for the corresponding discontinuous boundary conditions. Results from three numerical tests, including both straight and curved boundaries, are presented to show the accuracy and order of convergence of the LBE computations. Detailed error assessments are conducted for the interior temperature or concentration (denoted as a scalar ϕ) and the interior derivatives of ϕ for both types of boundary conditions, for the boundary flux in the Dirichlet problem and for the boundary ϕ values in the Neumann problem. When the discontinuity point on the straight boundary is placed at the center of the unit lattice in the Dirichlet problem, it yields only first-order accuracy for the interior distribution of ϕ, first-order accuracy for the boundary flux, and zeroth-order accuracy for the interior derivatives compared with the second-order accuracy of all quantities of interest for continuous boundary conditions. On the lattice scale, the LBE solution for the interior derivatives near the singularity is largely independent of the resolution and correspondingly the local distribution of the absolute errors is almost invariant with the changing resolution. For Neumann problems, when the discontinuity is placed at the lattice center, second-order accuracy is preserved for the interior distribution of ϕ; and a "superlinear" convergence order of 1.5 for the boundary ϕ values and first-order accuracy for the interior derivatives are obtained. For straight boundaries with the discontinuity point arbitrarily placed within the lattice and curved boundaries, the boundary flux becomes zeroth-order accurate for Dirichlet problems; and all three quantities, including the interior and boundary ϕ values and the interior derivatives, are only first-order accurate for Neumann problems.

DOI: 10.1103/PhysRevE.94.023307

I. INTRODUCTION

The lattice Boltzmann equation (LBE) method has become an effective alternative numerical method for heat and mass transfer modeling [1–21]. With the temperature and mass concentration considered as scalar variables, the governing equations for thermal and mass transport become a simple scalar convection-diffusion equation (CDE) [10–17]. For the energy equation, the viscous heat dissipation and pressure work terms can be conveniently incorporated as source terms [10–21]. Thus, the LBE method for CDE inherited the same benefits of the hydrodynamic version of the LBE: explicit algorithms, easy implementation, compatibility with parallelization, and ease of handling complex geometry.

Transport phenomena involving discontinuous boundary and interface conditions are frequently encountered in a wide range of science and engineering problems such as shock waves in acoustics and compressible viscous flows [22], diffusion of chemical reactants in porous catalyst pellets with partial external or internal wetted surfaces, or with nonuniform catalyst distribution and surface reaction (Ref. [23] and references therein), and heat conduction between two solids that have partial contact [24,25]. With analytical solutions available for only a limited number of transport problems with discontinuous boundary conditions, numerical methods become the only practical tool for most of the problems. The presence of discontinuities along the boundary or in the internal field (such as shock waves or hydraulic jumps) poses great challenges to any numerical method and is known to result in degradation of accuracy. In traditional finite-difference and finite-element based numerical computation of singularity problems, the singularity treatments can be categorized into three groups: the local refinement method, the singular function method, and the combined method (see [26–28] and references therein). The LBE method for hydrodynamic problems does not deal with internal shock waves since the method is only applicable to incompressible flows with nearly constant density and discontinuities in the velocity or pressure conditions along the boundary are rarely encountered.

For a physical variable ϕ when the discontinuity in the material properties occurs at an interface, jumps in ϕ and the normal derivative (flux) $\partial\phi/\partial n$ may develop across the interface. The pressure jump due to surface tension in two-phase flows and temperature derivative jump in conjugate heat transfer problems [20,29,30] are just two examples. For convenience, the type of discontinuity in ϕ and $\partial\phi/\partial n$ across the interface is hereinafter referred to as "normal discontinuity." Ginzburg and d'Humières [31] addressed Darcy's flow in anisotropic and heterogeneous stratified aquifers where mass conservation is described by a pure diffusion anisotropic equation. The heterogeneity of the cross-diffusion entries results in the discontinuous boundary derivatives when the physical (continuous) Neumann conditions are prescribed [31]. Discontinuous Neumann conditions across the inter-

[*]Corresponding author: likelichina@ufl.edu
[†]nauyeung@ufl.edu
[‡]rwmei@ufl.edu
[§]klaus@ufl.edu

face have been studied in [32] for both hydrodynamic and advection-diffusion equations. An interface treatment for heat and mass transfer with interfacial flux and/or temperature jumps has recently been proposed by Guo *et al.* [33] for conjugate heat and mass transfer problems. It was shown that the numerical accuracy of the LBE solutions is unaffected by the presence of the jumps in ϕ or $\partial\phi/\partial n$ across the interface, or the normal discontinuity.

To explore the applicability of the LBE method for heat and mass transfer problems with discontinuous Dirichlet and Neumann boundary conditions, we consider the effects of another important type of discontinuity, which is hereinafter referred as "tangential discontinuity." As the name suggests, the discontinuity in ϕ or $\partial\phi/\partial n$ occurs *along* the boundary, as opposed to *across* the interface in the normal discontinuity case. For heat and mass transfer problems, the tangential discontinuity occurs when ϕ or $\partial\phi/\partial n$ suddenly changes the value along the physical boundary. The understanding on the effects of tangential discontinuity on the accuracy of LBE solution will be of interest to researchers using LBE method for solving engineering problems. The specific questions the present paper attempts to address include: (i) How do the tangential type boundary condition discontinuities affect the order of accuracy of the LBE solution ϕ_{LBE} in the interior field for both Dirichlet and Neumann problems with straight walls? (ii) How do the tangential discontinuities affect the orders of accuracy of the interior derivatives and the boundary flux (or ϕ_w) values for the Dirichlet (or Neumann) problem? (iii) Does the placement of the tangential discontinuity point in the lattice affect the results in (i) and (ii)? (iv) How does convection affect the error behavior in (i) to (iii)? (v) What are the effects of tangential boundary condition discontinuities along curved walls on the accuracy of LBE results?

The rest of the paper is organized as follows. Section II briefly describes the LBE model for the general convection-diffusion equation governing thermal and mass transport processes. The boundary treatments for the Dirichlet and Neumann conditions with tangential discontinuous are presented in Sec. III, where the asymptotic distribution functions near the discontinuity are also derived. The error assessments and detailed examination of the effects of tangential discontinuities on the accuracy of the LBE solutions are presented in Sec. IV with three numerical tests, including both straight and curved boundaries. Section V summarizes the difference between the two types of discontinuity in LBE modeling. And some concluding remarks are given in Sec. VI.

II. LATTICE BOLTZMANN EQUATION FOR THERMAL AND MASS TRANSPORT

The macroscopic governing equation for thermal and mass transport can be written as a general convection-diffusion equation (CDE)

$$\frac{\partial\phi}{\partial t}+\frac{\partial}{\partial x_j}(v_j\phi)=\frac{\partial}{\partial x_i}\left(D_{ij}\frac{\partial\phi}{\partial x_j}\right)+G, \tag{1}$$

where ϕ is a scalar variable such as temperature in heat transfer or concentration in mass transfer problems, t is the time, v_j is the velocity component in the x_j direction, D_{ij} is the diffusion coefficient, and G is the general source term.

Of the various LBE models proposed in the literature [10–16] for the CDE (1), the multiple-relaxation-time (MRT) based D2Q5 (DnQm denotes m discrete lattice velocities in n dimensions) models proposed by Yoshida and Nagaoka [12] are used in the present work to formulate the transport problem since their second-order accuracy in space and first-order accuracy in time have been verified via a detailed asymptotic analysis. When presented in the moment space [17] the D2Q5 MRT-LBE model in [12] is very similar to the one used in [16]. The implementation of the D2Q5 model and the corresponding boundary condition treatment are much simpler compared to the D2Q9 models in [5,8,15]. It should also be noted that the boundary treatment applied in this work for the discontinuous boundary conditions is independent of the specific LBE models and it is also applicable to other LBE models.

In order to recover the macroscopic CDE (1), the following lattice Boltzmann equation for the evolution of the microscopic distribution function $g(\mathbf{x},\boldsymbol{\xi},t)$ was proposed in [12]

$$g_\alpha(\mathbf{x}+\mathbf{e}_\alpha\delta t,t+\delta t)-g_\alpha(\mathbf{x},t)=[L\mathbf{g}(\mathbf{x},t)]_\alpha+\omega_\alpha G(\mathbf{x},t)\delta t, \tag{2}$$

where $g_\alpha(\mathbf{x},t)\equiv g(\mathbf{x},\xi_\alpha,t)$, $\mathbf{x}$ is the spatial vector, $\boldsymbol{\xi}$ is the particle velocity vector in the phase space $(\mathbf{x},\boldsymbol{\xi})$ and it is discretized to a small set of discrete velocities $\{\boldsymbol{\xi}_\alpha|\alpha=0,1,\ldots,m-1\}$, $\mathbf{e}_\alpha$ is the αth discrete velocity vector [$\{\mathbf{e}_\alpha\}=(0,0),(\pm1,0)$, and $(0,\pm1)$ for D2Q5], δt is the time step, L is the standard collision operator in the LBE method, and ω_α is the weight coefficient.

For MRT-based LBE models, it is more natural to represent the collision operator in the moment space as [34]

$$L\mathbf{g}(\mathbf{x},t)=-M^{-1}S[\mathbf{m}(\mathbf{x},t)-\mathbf{m}^{(\mathrm{eq})}(\mathbf{x},t)], \tag{3a}$$

where M is a matrix to transform the distribution functions $\mathbf{g}$ to their moments $\mathbf{m}$ by $\mathbf{m}=M\mathbf{g}$, and S is a matrix of relaxation coefficients τ_{ij}. To recover the CDE (1), the equilibrium moments of the distribution functions are defined in [11,14,16,17] as

$$\mathbf{m}^{(\mathrm{eq})}=(0,u\phi,v\phi,a\phi,0)^T, \tag{3b}$$

where u and v are the macroscopic velocity components in Cartesian coordinates. For the D2Q5 model used in this work for isotropic convection-diffusion, the matrices are [35,12]

$$M=\begin{bmatrix}1&1&1&1&1\\0&1&-1&0&0\\0&0&0&1&-1\\4&-1&-1&-1&-1\\0&1&1&-1&-1\end{bmatrix},$$

$$S^{-1}=\begin{bmatrix}\tau_0&0&0&0&0\\0&\tau_{11}&0&0&0\\0&0&\tau_{22}&0&0\\0&0&0&\tau_3&0\\0&0&0&0&\tau_4\end{bmatrix}, \tag{3c}$$

and $\omega_0=1/3$, $\omega_\alpha=1/6$ $(\alpha=1,2,3,4)$, and $a=(5\omega_0-1)=2/3$. In particular, when $\tau_0=0$, $\tau_{11}=\tau_{22}=\tau_D$, $\tau_3=\tau_4=\tau_p$, the MRT model reduces to two-relaxation-time (TRT) model [13,32].

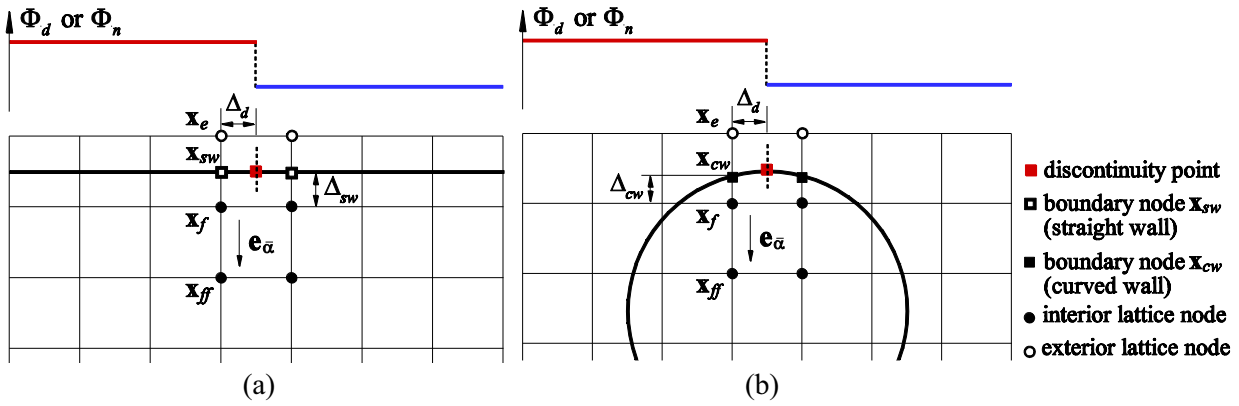

FIG. 1. Illustration of the placement of (a) a straight wall and (b) a curved boundary wall in the square lattice. The imposed Dirichlet (Φ_d) or Neumann (Φ_n) boundary condition has a discontinuity along the boundary in the tangential direction (horizontal in the figures). The location of the discontinuity point in the lattice along the horizontal direction is indicated by Δ_d; the intersection link fractions in the lattice velocity vector $\mathbf{e}_{\bar{\alpha}}$ direction (vertical in the figure) are $\Delta_{\rm sw} = \|\mathbf{x}_f - \mathbf{x}_{\rm sw}\|/\|\mathbf{x}_f - \mathbf{x}_e\|$ for the boundary node $\mathbf{x}_{\rm sw}$ on the straight wall, and $\Delta_{\rm cw} = \|\mathbf{x}_f - \mathbf{x}_{\rm cw}\|/\|\mathbf{x}_f - \mathbf{x}_e\|$ for the boundary node $\mathbf{x}_{\rm cw}$ on the curved wall.

The asymptotic analysis in [12] showed that the leading-order solution of the CDE (1) is obtained from the moment of the distribution functions

$$\phi(\mathbf{x},t) = \sum_{\alpha=0}^{m-1} g_\alpha(\mathbf{x},t), \tag{4}$$

with second-order accuracy in space and first-order accuracy in time when the following relationship is preserved:

$$\tau_{ij} = \frac{1}{2}\delta_{ij} + \frac{\delta t}{\varepsilon_D(\delta x)^2} D_{ij}, \tag{5}$$

where δ_{ij} is the Kronecker delta and the constant $\varepsilon_D = 1/3$ in D2Q5.

For computation and memory efficiency, the evolution equation (2) with the MRT collision operator in Eq. (3) is usually solved in two steps

collision step:

$$\hat{g}_\alpha(\mathbf{x},t) = g_\alpha(\mathbf{x},t) - \{M^{-1}S[\mathbf{m}(x,t) - \mathbf{m}^{(\rm eq)}(\mathbf{x},t)]\}_\alpha + \omega_\alpha G(\mathbf{x},t)\delta t, \tag{6}$$

streaming step:

$$g_\alpha(\mathbf{x} + \mathbf{e}_\alpha\delta t, t + \delta t) = \hat{g}_\alpha(\mathbf{x},t), \tag{7}$$

where $\hat{g}_\alpha$ represents the post-collision state. It is noted that an efficient implementation of the collision step does not require the storage of $\hat{g}_\alpha$. The collision step in Eq. (6) is completely local and the streaming step in Eq. (7) is simple and requires little computational effort.

III. BOUNDARY TREATMENT FOR DISCONTINUOUS BOUNDARY CONDITIONS

Accurate implementation of hydrodynamic or thermal boundary conditions by converting the macroscopic physical variables on the boundary into corresponding microscopic distribution functions in the LBE methods has been of significant interest since the LBE method has been proposed. The boundary schemes are typically constructed in such a way that the boundary velocity, temperature, or heat flux obtained from the LBE computation matches the respective physical boundary condition to a certain degree of accuracy. A short review of the boundary treatments for hydrodynamic and thermal and mass transport modeling involving straight and curved boundaries was given by Li *et al.* [17].

The tangential-type discontinuous boundary condition on straight and curved boundary walls and the placement of the discontinuity points in the square lattice of unit spacing ($\delta x = \delta y = 1$) are schematically depicted in Fig. 1. To avoid the numerical involvement of double values at the exact discontinuity point, we place the discontinuity point between two lattice nodes along the tangential direction of the boundary ($\Delta_d \neq 0$ in the x direction in Fig. 1) so that the boundary condition at the discontinuity point is not needed. In the normal direction (see vector $\mathbf{e}_{\bar{\alpha}}$ in Fig. 1), the intersection link fractions are $\Delta_{\rm sw} = \|\mathbf{x}_f - \mathbf{x}_{\rm sw}\|/\|\mathbf{x}_f - \mathbf{x}_e\|$ for the boundary node $\mathbf{x}_{\rm sw}$ on the straight wall, and $\Delta_{\rm cw} = \|\mathbf{x}_f - \mathbf{x}_{\rm cw}\|/\|\mathbf{x}_f - \mathbf{x}_e\|$ for the boundary node $\mathbf{x}_{\rm cw}$ on the curved wall.

In the LBE method, the evolution equation (2) governs the behavior of the microscopic distribution functions $\mathbf{g}(\mathbf{x},t)$ at the interior of the computational domain. To complete the streaming step in Eq. (7), a boundary treatment is required to convert the macroscopic boundary information, such as a Dirichlet boundary value (Φ_d), a Neumann boundary flux (Φ_n), or their combination (the mixed boundary condition) at the boundary node ($\mathbf{x}_{\rm sw}$ or $\mathbf{x}_{\rm cw}$ in Fig. 1), into appropriate boundary conditions for $\mathbf{g}(\mathbf{x},t)$ at the first interior lattice node ($\mathbf{x}_f$ in Fig. 1) adjacent to the boundary node.

With the placement of the discontinuity point between the lattice nodes, the regular boundary treatments can be directly applied. The second-order accurate boundary treatment by Li *et al.* [17] based on the "(anti)-bounce-back" idea and spatial interpolation is capable of preserving the exact local geometry and can be extended to curved boundary situations. These boundary schemes for Dirichlet and Neumann conditions are thus used in this work.

A. Discontinuous Dirichlet condition treatment

For the macroscopic Dirichlet condition $\phi = \Phi_d$ at the boundary node $\mathbf{x}_w$ ($\mathbf{x}_{\rm sw}$ or $\mathbf{x}_{\rm cw}$ in Fig. 1), the distribution function at the first interior lattice node $\mathbf{x}_f$ along the lattice

velocity direction $\mathbf{e}_{\bar{\alpha}}$ (see Fig. 1) at the current time $t+\delta t$, can be expressed as [17]

$$g_{\bar{\alpha}}(\mathbf{x}_f,t+\delta t) = c_{d1}\hat{g}_{\alpha}(\mathbf{x}_f,t) + c_{d2}\hat{g}_{\alpha}(\mathbf{x}_{ff},t) + c_{d3}\hat{g}_{\bar{\alpha}}(\mathbf{x}_f,t) + c_{d4}\varepsilon_D\Phi_d, \quad (8)$$

where $\mathbf{x}_{ff}$ is the second interior lattice node along $\mathbf{e}_{\bar{\alpha}}$ direction, i.e., $\mathbf{x}_{ff}=\mathbf{x}_f+\mathbf{e}_{\bar{\alpha}}\delta t$, and c_{d1}–c_{d4} are coefficients related to the local link fraction Δ (Δ_{sw} or Δ_{cw} in Fig. 1). The asymptotic analysis in [17] showed that second-order accuracy is preserved for the Dirichlet boundary condition with treatment (8) when the following relationship is maintained, with $c_{d1}(\neq 1)$ an adjustable variable:

$$c_{d2} = -\frac{2\Delta c_{d1}+1}{2\Delta+1},$$
$$c_{d3} = \frac{c_{d1}+2\Delta}{2\Delta+1}, \quad \text{and} \quad c_{d4} = \frac{-c_{d1}+1}{2\Delta+1}. \quad (9)$$

Three particular schemes were examined in [17] and they all reduce to the anti-bounce-back scheme at $\Delta=0.5$.

Scheme 1:

$$g_{\bar{\alpha}}(\mathbf{x}_f,t+\delta t) = \begin{cases} (-2\Delta)\hat{g}_{\alpha}(\mathbf{x}_f,t) + (2\Delta-1)\hat{g}_{\alpha}(\mathbf{x}_{ff},t) + \varepsilon_D\Phi_d, & (0\leqslant\Delta\leqslant 0.5), \\ \left(-\frac{1}{2\Delta}\right)\hat{g}_{\alpha}(\mathbf{x}_f,t) + \left(1-\frac{1}{2\Delta}\right)\hat{g}_{\bar{\alpha}}(\mathbf{x}_f,t) + \left(\frac{1}{2\Delta}\right)\varepsilon_D\Phi_d, & (\Delta>0.5), \end{cases} \quad (10a)$$

Scheme 2:

$$g_{\bar{\alpha}}(\mathbf{x}_f,t+\delta t) = 2(\Delta-1)\hat{g}_{\alpha}(\mathbf{x}_f,t) - \left(\frac{(2\Delta-1)^2}{2\Delta+1}\right)\hat{g}_{\alpha}(\mathbf{x}_{ff},t) + 2\left(\frac{2\Delta-1}{2\Delta+1}\right)\hat{g}_{\bar{\alpha}}(\mathbf{x}_f,t) + \left(\frac{3-2\Delta}{2\Delta+1}\right)\varepsilon_D\Phi_d, \quad (10b)$$

Scheme 3:

$$g_{\bar{\alpha}}(\mathbf{x}_f,t+\delta t) = -\hat{g}_{\alpha}(\mathbf{x}_f,t) + \left(\frac{2\Delta-1}{2\Delta+1}\right)\hat{g}_{\alpha}(\mathbf{x}_{ff},t) + \left(\frac{2\Delta-1}{2\Delta+1}\right)\hat{g}_{\bar{\alpha}}(\mathbf{x}_f,t) + \left(\frac{2}{2\Delta+1}\right)\varepsilon_D\Phi_d. \quad (10c)$$

B. Discontinuous Neumann condition treatment

For the Neumann (flux) boundary condition $-D_n\frac{\partial\phi}{\partial n}=\Phi_n$ at $\mathbf{x}_w$ in the normal direction, the second-order accurate boundary condition treatment proposed in [17] is

$$g_{\bar{\alpha}}(\mathbf{x}_f,t+\delta t) = c_{n1}\hat{g}_{\alpha}(\mathbf{x}_f,t) + c_{n2}\hat{g}_{\alpha}(\mathbf{x}_{ff},t) + c_{n3}\hat{g}_{\bar{\alpha}}(\mathbf{x}_f,t) + c_{n4}\frac{\delta t}{\delta x}\Phi_{n\bar{\alpha}}, \quad (11)$$

where it should be noted that $\Phi_{n\bar{\alpha}}$ is the boundary flux along the lattice velocity $\mathbf{e}_{\bar{\alpha}}$ direction. The asymptotic analysis in [17] showed that the coefficients $c_{n1}-c_{n4}$ in Eq. (11) are unique for second-order accuracy. The boundary scheme can be written as

$$g_{\bar{\alpha}}(\mathbf{x}_f,t+\delta t) = \hat{g}_{\alpha}(\mathbf{x}_f,t) - \frac{2\Delta-1}{2\Delta+1}\hat{g}_{\alpha}(\mathbf{x}_{ff},t) + \frac{2\Delta-1}{2\Delta+1}\hat{g}_{\bar{\alpha}}(\mathbf{x}_f,t) + \frac{2}{2\Delta+1}\frac{\delta t}{\delta x}\Phi_{n\bar{\alpha}}. \quad (12)$$

As emphasized in [17,18], when the local boundary normal $\mathbf{n}$ is aligned with $\mathbf{e}_{\bar{\alpha}}$ [e.g., boundary node $\mathbf{x}_{sw}$ in Fig. 1(a)], $\Phi_{n\bar{\alpha}}=\Phi_n$ and thus Eq. (12) can be directly applied. When $\mathbf{n}$ is not in the $\mathbf{e}_{\bar{\alpha}}$ direction [boundary node $\mathbf{x}_{cw}$ in Fig. 1(b)], which is usually encountered on inclined or curved boundaries, $\Phi_{n\bar{\alpha}}$ is not equal to Φ_n and also depends on the unknown tangential flux. A Cartesian decomposition method proposed in [17] should be used to obtain $\Phi_{n\bar{\alpha}}$ based on Φ_n. For details about the Neumann condition treatment for curved boundaries and its extension to mixed boundary conditions please refer to [17].

C. Evaluation of boundary flux and boundary value and interior derivatives

To gain a full understanding on the effects of the tangential-type boundary condition discontinuities on the accuracy of LBE solutions, we also assess the accuracy of the boundary flux (or boundary temperature and concentration values) for given Dirichlet (or Neumann) problems. In addition, the interior derivatives for both types of problems are assessed. These quantities can be obtained from the microscopic distribution functions using the techniques proposed in [17,18] without any finite-difference calculations that are based on the computed values of the macroscopic temperature and concentration field.

Combining the boundary schemes in Eqs. (8) and (11) with the coefficients in Eqs. (9) and (12), the boundary flux for a Dirichlet problem can be evaluated from [17]

$$\Phi_{n\bar{\alpha}} = \left(\frac{1-c_{d1}}{2}\right)\frac{\delta x}{\delta t}\left[-(2\Delta+1)\hat{g}_{\alpha}(\mathbf{x}_f,t) + \left(2\Delta-\frac{2}{1-c_{d1}}\right)\hat{g}_{\alpha}(\mathbf{x}_{ff},t) + \left(\frac{2}{1-c_{d1}}-1\right)\times\hat{g}_{\bar{\alpha}}(\mathbf{x}_f,t) + \varepsilon_D\Phi_d\right], \quad (13)$$

and the boundary temperature (concentration) for a Neumann problem can be evaluated using [17]

$$\Phi_d = \frac{1}{\varepsilon_D}\left[(2\Delta+1)\hat{g}_{\alpha}(\mathbf{x}_f,t) + \left(\frac{2}{1-c_{d1}}-2\Delta\right)\hat{g}_{\alpha}(\mathbf{x}_{ff},t) + \left(1-\frac{2}{1-c_{d1}}\right)\hat{g}_{\bar{\alpha}}(\mathbf{x}_f,t) + \left(\frac{2}{1-c_{d1}}\right)\frac{\delta t}{\delta x}\Phi_{n\bar{\alpha}}\right]. \quad (14)$$

For both Dirichlet and Neumann problems, the interior derivatives can be obtained using [12,18]

$$-\tau_{ij}\frac{\partial\phi}{\partial x_j}=\frac{1}{\varepsilon_D\delta x}\sum_{\alpha=1}^{m-1}e_{\alpha i}g_\alpha^{(\mathrm{neq})}, \tag{15a}$$

where $g_\alpha^{(\mathrm{neq})}=g_\alpha-g_\alpha^{(\mathrm{eq})}$ is the nonequilibrium component of the distribution function with $g_\alpha^{\mathrm{eq}}(\mathbf{x},t)=(\omega_\alpha+\frac{\delta t v_j}{\delta x\varepsilon_D}e_{\alpha j}\omega_\alpha)\phi(\mathbf{x},t)$ [12]. For isotropic diffusion in 2D cases ($D_{xx}=D_{yy}=D$, $\tau_{xx}=\tau_{yy}=\tau_D$), the following can be obtained from Eq. (15a) [18]:

$$-D\frac{\partial\phi}{\partial x}=\left(1-\frac{1}{2\tau_D}\right)\left(\frac{\delta x}{\delta t}\right)\sum_{\alpha=1}^{4}e_{\alpha x}g_\alpha^{(\mathrm{neq})},$$

$$-D\frac{\partial\phi}{\partial y}=\left(1-\frac{1}{2\tau_D}\right)\left(\frac{\delta x}{\delta t}\right)\sum_{\alpha=1}^{4}e_{\alpha y}g_\alpha^{(\mathrm{neq})}. \tag{15b}$$

The second-order accuracy of the schemes given by Eqs. (13)–(15) has been verified in [17,18] for continuous boundary conditions.

D. Analysis of the microscopic distribution functions near the discontinuity

The effect of the discontinuous boundary conditions on the accuracy of the LBE computations is more severe in the local region near the discontinuity. To understand the causes for the deteriorated accuracy, we also investigate the errors in the simulated microscopic distribution functions with regard to their asymptotic values. Following the asymptotic analysis, e.g., in Ref. [12], the micro- and macroscopic quantities can be expressed as $g_\alpha=g_\alpha^{(0)}+\epsilon g_\alpha^{(1)}+\epsilon^2 g_\alpha^{(2)}+\cdots$, and $\phi=\phi^{(0)}+\epsilon\phi^{(1)}+\epsilon^2\phi^{(2)}+\cdots$, respectively, where $\epsilon=\delta x/L$ is the small parameter with L the characteristic length. With the presently implemented LB model, the following second-order asymptotic distribution functions ($g_\alpha=g_{\alpha\_\mathrm{asymptotic}}+\epsilon^2 g_\alpha^{(2)}+\cdots$) can be readily derived

$$g_{\alpha\_\mathrm{asymptotic}}=\left[\omega_\alpha\left(\phi^{(0)}+\frac{\delta t}{\delta x}\frac{v_j}{\varepsilon_D}e_{\alpha j}\phi^{(0)}\right)-\omega_\alpha\tau_D e_{\alpha j}\frac{\partial\phi^{(0)}}{\partial x_j}\right]. \tag{16}$$

Thus one can examine the errors for the individual distribution functions $\gamma_\alpha=g_{\alpha\_\mathrm{LBE}}-g_{\alpha\_\mathrm{asymptotic}}$ by replacing $\phi^{(0)}$ in Eq. (16) with the exact solution ϕ_{ex}. Moreover, the error transfer from the microscopic distribution functions to the macroscopic ϕ value and its derivatives can be clearly analyzed. For isotropic 2D diffusion problems, the following expressions for the absolute errors can be obtained:

$$E_\phi=\sum_{\alpha=0}^{4}\gamma_\alpha,$$

$$E_{\partial\phi/\partial x}=\kappa\sum_{\alpha=1}^{4}e_{\alpha x}\gamma_\alpha,$$

$$\text{and}\quad E_{\partial\phi/\partial y}=\kappa\sum_{\alpha=1}^{4}e_{\alpha y}\gamma_\alpha, \tag{17}$$

according to Eqs. (4) and (15b), respectively, with $\kappa=-1/(\tau_D\varepsilon_D)$.

IV. NUMERICAL TESTS AND DISCUSSION

Three numerical tests are conducted in this study to investigate the effects of the tangential-type discontinuous boundary conditions on the accuracy of the LBE computations. The first test is for heat conduction in a square block. The second involves convection-diffusion in a channel with straight boundaries. And the third test deals with a curved boundary for heat conduction in a circle. All the tests are steady-state problems, and both the Dirichlet and Neumann boundary conditions with tangential discontinuities are considered. For all cases, only isotropic diffusion is considered thus $\tau_{ij}=\tau_D\delta_{ij}$ [see Eq. (5)] throughout the domain. It is worth noting that according to [13,32,36], the coefficient of the convergence curves is determined by the combination $\Lambda=(\tau_D-0.5)(\tau_p-0.5)$. This is also verified in this study with numerical tests including both continuous and discontinuous boundary conditions. For all the results shown below, a specific choice of $\tau_D=0.75$ and $\tau_p=1.0$ with $\Lambda=1/8$ is thus used for most cases unless stated otherwise. It should be noted that as shown in Refs. [36,37], the choice of $\Lambda=1/8$ is equivalent to extending the second-order accuracy of the anti-bounce-back scheme to the third order for straight boundaries located halfway in the lattice ($\Delta=0.5$). While this analysis is more sophisticated and complex than the second-order asymptotic analysis in [12], the numerical evidence of the superiority of using the recommended value $\Lambda=1/8$ in this work will be demonstrated in the presence of strong discontinuity.

A. Heat conduction in a square block

The placement of the lattices on the square block ($H=L$) is shown in Fig. 2. The boundary conditions on the right, top, and bottom walls are fixed with $\phi_w=0$. On the left wall, a

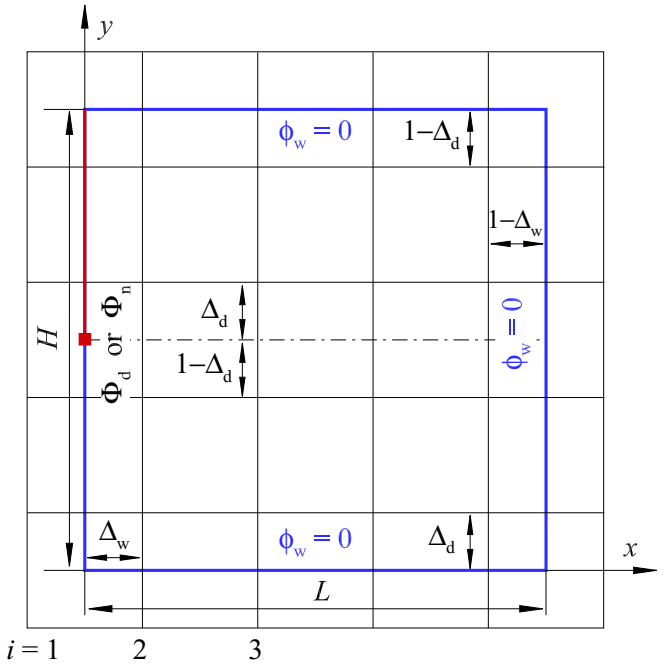

FIG. 2. Schematic depiction of the computational domain and lattice distribution for the square diffusion problem.

tangential-type discontinuous boundary condition is imposed and the discontinuity is fixed at $y = H/2$. The variations in Δ_d and Δ_w are realized by moving the whole block in the lattice. The exact solution to the steady conduction equation in the block subject to the continuous boundary condition $\phi_w = 0$ on the three walls can be written as

$$\phi_{\rm ex}(x,y) = \phi_{\rm ex}(\xi,\eta) = \sum_{n=1}^{\infty} \beta_n \sin(n\pi\eta)\sinh[n\pi(\xi - L/H)];$$
$$\xi = x/H; \quad \eta = y/H, \tag{18}$$

where the coefficients β_n are to be determined from the specific boundary condition on the left wall.

1. Discontinuous Dirichlet boundary condition

a. Analytical solutions. When the Dirichlet condition on the left wall is given as

$$\phi(\xi = 0,\eta) = f(\eta), \tag{19}$$

the exact solution in Eq. (16) becomes

$$\phi_{\rm ex}(\xi,\eta) = 2\sum_{n=1}^{\infty} b_n \sin(n\pi\eta)\frac{\sinh[n\pi(\xi - L/H)]}{\sinh(-n\pi L/H)}, \tag{20a}$$

with

$$b_n \equiv \int_0^1 f(\eta)\sin(n\pi\eta)d\eta. \tag{20b}$$

Three different types of discontinuous functions $f(\eta)$ are examined in this study,

$$\text{piecewise linear}: f(\eta) = f_{\rm linear}(\eta) = \begin{cases}\eta, & \eta < 1/2,\\ \eta - 1, & \eta > 1/2,\end{cases} \tag{21a}$$

$$\text{piecewise parabolic}: f(\eta) = f_{\rm parab}(\eta) = \begin{cases}2\eta(1-\eta), & \eta < 1/2,\\ -2\eta(1-\eta), & \eta > 1/2,\end{cases} \tag{21b}$$

$$\text{piecewise sine}: f(\eta) = f_{\rm sine}(\eta) = \begin{cases}\frac{1}{2}\sin(\pi\eta), & \eta < 1/2,\\ -\frac{1}{2}\sin(\pi\eta), & \eta > 1/2.\end{cases} \tag{21c}$$

The jump magnitudes of all three functions at $\eta = 1/2$ are unity. It should be noted that for relatively large values of n (say $n \geqslant 10$), the absolute values of both $\sinh[n\pi(\xi - L/H)]$ and $\sinh(-n\pi L/H)$ in Eq. (20a) are exponentially large and direct division of the "sinh" values yields poor numerical accuracy that is unsuited for the present work. Thus Eq. (20a) is rewritten as

$$\phi_{\rm ex}(\xi,\eta) = 2\sum_{n=1}^{M} b_n \sin(n\pi\eta)\frac{\sinh[n\pi(\xi - L/H)]}{\sinh(-n\pi L/H)} + 2\sum_{n=M+1}^{N_\infty} b_n \sin(n\pi\eta)[e^{-n\pi\xi} - e^{n\pi(\xi-2L/H)}]. \tag{22}$$

In the present computations, $M = 10$ is used; the error in approximating $e^{-2M\pi}$ (with $L = H$) as zero is less than 10^{-27}. Large values of N_∞ are used for small ξ so that the relative error resulting from the truncation of the series such as given by Eq. (22) is less than 10^{-16}.

The derivatives in the field, $0 < \xi \leq L/H$, $0 \leq \eta \leq 1$, are obtained from the exact solution

$$\frac{\partial\phi_{\rm ex}}{\partial\xi} = 2\pi\sum_{n=1}^{M} b_n n \sin(n\pi\eta)\frac{\cosh[n\pi(\xi - L/H)]}{\sinh(-n\pi L/H)} - 2\pi\sum_{n=M+1}^{N_\infty} b_n n \sin(n\pi\eta)[e^{-n\pi\xi} + e^{n\pi(\xi-2L/H)}], \tag{23a}$$

$$\frac{\partial\phi_{\rm ex}}{\partial\eta} = 2\pi\sum_{n=1}^{M} b_n n \cos(n\pi\eta)\frac{\sinh[n\pi(\xi - L/H)]}{\sinh(-n\pi L/H)} + 2\pi\sum_{n=M+1}^{N_\infty} b_n n \cos(n\pi\eta)[e^{-n\pi\xi} - e^{n\pi(\xi-2L/H)}]. \tag{23b}$$

On the left wall ($\xi = 0$), $\partial\phi_{\rm ex}(0,\eta)/\partial\eta$ can be evaluated directly from the Dirichlet boundary condition given by Eq. (21) without the need of Eq. (23b). For $\partial\phi_{\rm ex}(0,\eta)/\partial\xi$, one cannot set $\xi = 0$ in Eq. (23a) since the series solution does not converge at $\xi = 0$ in its current form. To obtain a reliable normal derivative at $\xi = 0$, a fourth-order accurate extrapolation is applied using $\partial\phi_{\rm ex}/\partial\xi$ values near $\xi = 0$ at $\xi = \varepsilon$, 2ε, 3ε, and 4ε evaluated from Eq. (23a), i.e.,

$$\left.\frac{\partial\phi_{\rm ex}}{\partial\xi}\right|_{\xi=0} \cong 4\left.\frac{\partial\phi_{\rm ex}}{\partial\xi}\right|_{\xi=\varepsilon} - 6\left.\frac{\partial\phi_{\rm ex}}{\partial\xi}\right|_{\xi=2\varepsilon} + 4\left.\frac{\partial\phi_{\rm ex}}{\partial\xi}\right|_{\xi=3\varepsilon} - \left.\frac{\partial\phi_{\rm ex}}{\partial\xi}\right|_{\xi=4\varepsilon} - \frac{\partial^5\phi_{\rm ex}}{\partial\xi^5}\varepsilon^4. \tag{24}$$

The $O(\varepsilon^4)$ term is not included in the actual computation; it is shown here to illustrate the extrapolation error. For very small ξ or ε, the series in Eq. (23a) converges very slowly. Shanks transformation [38] is used to accelerate the convergence of the series. For $f = f_{\rm linear}(\eta)$, extremely high accuracy is needed for $\partial\phi_{\rm ex}/\partial\xi$ in assessing the LBE solution accuracy and very small ε is desired. In this case, quadruple precision (with at least 33 significant decimal digits) is used to further reduce the round-off errors. To assess the truncation error in Eq. (24) and to interpret the behavior of the LBE solution errors, it is important to understand the behavior of the derivatives near the left wall, especially near the discontinuity point.

Since $\phi_{\rm ex}(\xi,\eta)$ is a harmonic function, its derivatives $(\partial\phi_{\rm ex}/\partial\xi, \partial\phi_{\rm ex}/\partial\eta)$ are also harmonic. The local solution may be constructed using elementary functions for the Laplace equation. Further using the numerical values for $(\partial\phi_{\rm ex}/\partial\xi, \partial\phi_{\rm ex}/\partial\eta)$ computed from Eq. (23), the leading asymptotic behavior of the derivatives near the discontinuity $(\xi = 0, \eta = 1/2)$ can be obtained for $f = f_{\rm linear}(\eta)$, as

$$\frac{\partial\phi_{\rm ex}}{\partial\xi} \sim \frac{1}{\pi}\frac{\eta - 0.5}{\xi^2 + (\eta - 0.5)^2} - 1.0471(\eta - 0.5), \tag{25a}$$

$$\frac{\partial\phi_{\rm ex}}{\partial\eta} \sim -\frac{1}{\pi}\frac{\xi}{\xi^2 + (\eta - 0.5)^2} + 1 - 1.0471\xi. \tag{25b}$$

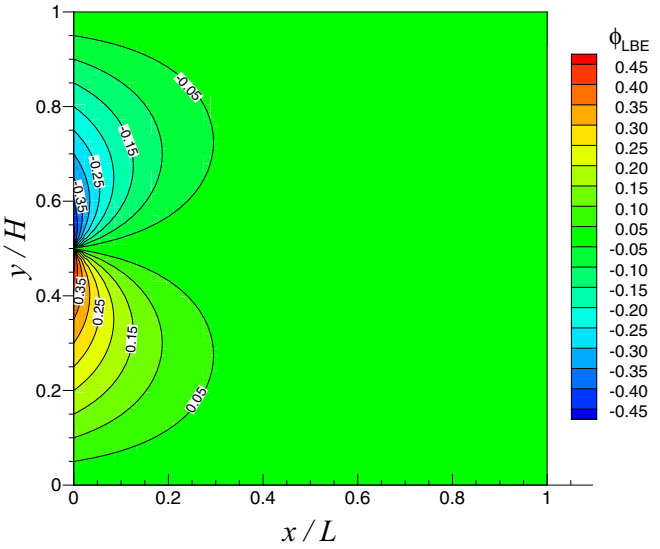

FIG. 3. Contours of ϕ_{LBE} at $H = L = 64$ with the discontinuous Dirichlet boundary condition $f_{\mathrm{linear}}(\eta)$ [Eq. (21a)] on the left wall ($\Delta_d = \Delta_w = \Delta = 0.5$ and the anti-bounce-back scheme is used).

The singular terms in the above describe the behavior of a vertically oriented dipole for $\partial\phi_{\mathrm{ex}}/\partial\xi$ and a horizontally oriented dipole for $\partial\phi_{\mathrm{ex}}/\partial\eta$ if the derivatives are viewed as electric potentials. For convenience, the local solutions given by the entire right-hand-side (RHS) of Eq. (25) are simply referred to as "dipole models" hereinafter. The phrase "singular term" will refer to the first term in each of Eqs. (25a) and (25b). For $f = f_{\mathrm{parab}}(\eta)$ and $f = f_{\mathrm{sine}}(\eta)$, the leading singular terms are identical to the above because the dipole strength is dictated by the jump magnitude. The differences among the solutions corresponding to the three forms given by Eqs. (21a)–(21c) are in the nonsingular terms which have only high-order effects.

From Eq. (25a),

$$\left.\frac{\partial^5\phi_{\mathrm{ex}}}{\partial\xi^5}\right|_{\xi=0} \sim \frac{24}{\pi}\left(\eta - \frac{1}{2}\right)^{-5}.$$

For $H = 202$ in the lattice scale and $\Delta_d = 0.5$, $\frac{\partial^5\phi_{\mathrm{ex}}}{\partial\xi^5} \sim 8.22 \times 10^{13}$ at $\xi = 0$, $\eta - 0.5 = 1/(2H)$. Using $\varepsilon = 10^{-6}$, the maximum extrapolation error in using Eq. (24) for $H = 202$ is 8.22×10^{-11}. Since $|\frac{\partial^5\phi_{\mathrm{ex}}}{\partial\xi^5}|$ and the corresponding truncation error in Eq. (24) decrease rapidly away from the singularity, Eq. (24) is sufficient for normal derivative evaluation on the wall in the present work dealing with finite jump discontinuities.

b. LBE solution contours and profiles. We first investigate the effect of the tangential-type discontinuous boundary condition on the LBE solutions by placing the discontinuity point at the center of the unit lattice, i.e., $\Delta_d = \Delta_w = \Delta = 0.5$ (see Fig. 2) is used for all four boundary walls in the results shown in Figs. 3–8. Thus the thermal anti-bounce-back scheme, which is recovered by all three schemes in Eqs. (10a)–(10c), is applied. For the LBE results in Figs. 3 and 4, $H = 64$ is used. For illustration purposes, Fig. 3 shows the contours of ϕ_{LBE} for $f = f_{\mathrm{linear}}(\eta)$. Very similar distributions are noted for the other two forms of $f(\eta)$ and are thus not shown for brevity. Figures 4(a) and 4(b) show the contours for the derivatives $\frac{\partial\phi}{\partial x}(= \frac{1}{H}\frac{\partial\phi}{\partial\xi})$ and $\frac{\partial\phi}{\partial y}(= \frac{1}{H}\frac{\partial\phi}{\partial\eta})$ from the LBE solutions. The magnitude of the derivatives in the vicinity of the discontinuity is much larger than that in the rest of the field due to the presence of the singularity in the derivatives. The contours show that $\partial\phi/\partial x$ is dominated by a vertically oriented dipole (or doublet) and $\partial\phi/\partial y$ by a horizontally oriented dipole of the same strength, as the leading order terms in Eq. (25) suggest. Figure 5 compares the normal derivative $\partial\phi/\partial x$ on the upper half of the left wall $x = 0$ between the exact and LBE solutions for all three cases; the lower half is antisymmetric with respect to $y/H = 0.5$. Also shown is the dipole model

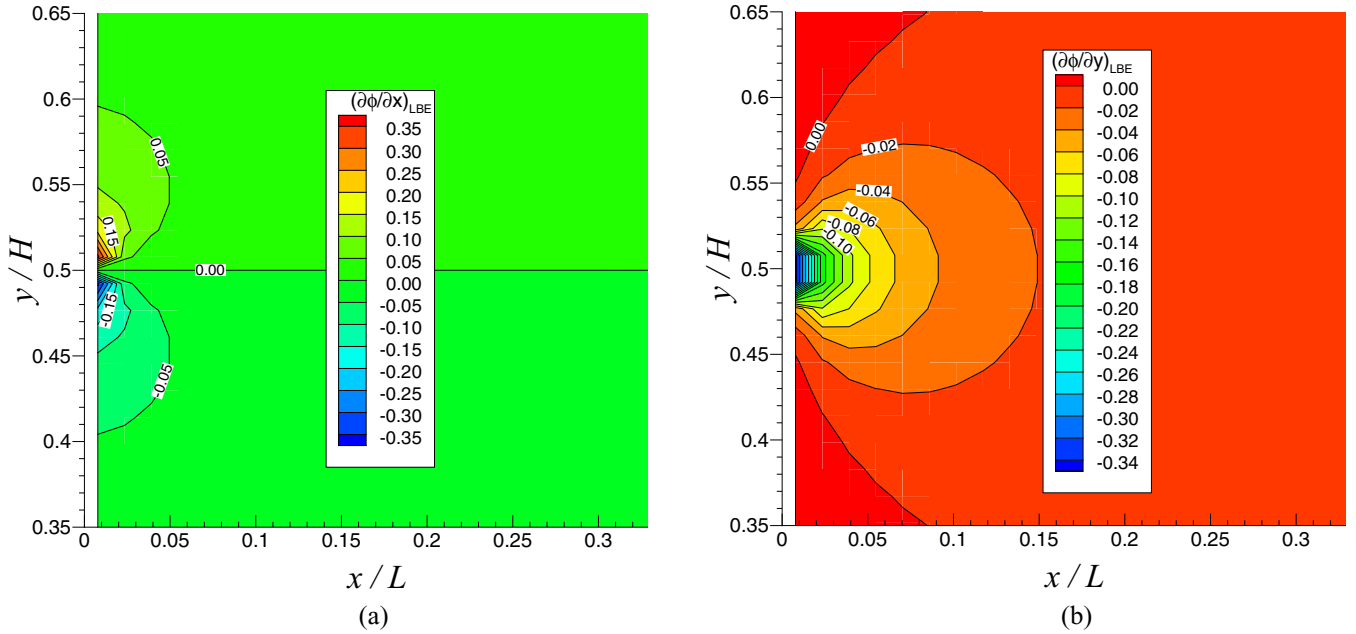

FIG. 4. Contours of interior derivatives (a) $\partial\phi/\partial x$ and (b) $\partial\phi/\partial y$ near the discontinuity point at $H = L = 64$ with $f_{\mathrm{linear}}(\eta)$ on the left wall.

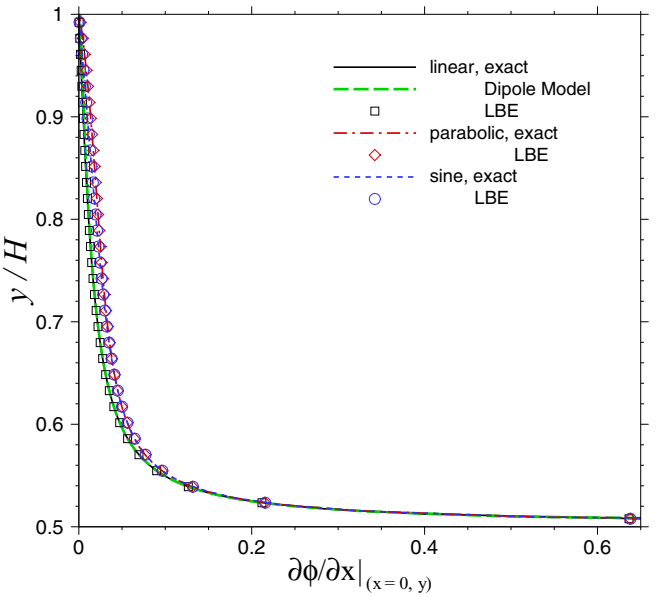

FIG. 5. Comparisons of $\partial\phi/\partial x$ on the left wall for $H = 64$, $\tau_D = 0.75$, and $D = 1/12$ between exact and LBE solutions for three discontinuous Dirichlet conditions given by Eqs. (21a)–(21c). The result from the dipole model is for the linear case $f_{\text{linear}}(\eta)$.

given by Eq. (25a) for $f = f_{\text{linear}}(\eta)$. Excellent agreement is observed for the wall normal derivative between the LBE and the exact solutions, and between the dipole mode and the exact solution for $f = f_{\text{linear}}(\eta)$. This analysis gives credence to the dipole model for its simple and accurate description of the singular behavior of the derivatives.

c. Invariance of the error for interior derivative with resolution. In discussing the accuracy of the derivatives, $\partial\phi/\partial x$ and $\partial\phi/\partial y$ are used in this study as opposed to $\partial\phi/\partial\xi$ and $\partial\phi/\partial\eta$ since for a given $f(\eta)$, it is observed that $\partial\phi/\partial x$ and $\partial\phi/\partial y$ remain almost the same on the lattice scale as the resolution H changes. Figures 6(a) and 6(b) show vertical distributions of $\partial\phi/\partial x$ and $\partial\phi/\partial y$ of the LBE solutions for $H = 32$, 48, 64, and 128 on the lattice scale for $i = 2$, 3, and 4 using $f = f_{\text{linear}}(\eta)$. The LBE solutions near the singular point $(x, y) = (0, H/2)$ with different resolution H are almost identical for $\partial\phi/\partial x$. The leading order behavior of $\partial\phi/\partial y$ remains the same as H changes from 32 to 128; the spread in $\partial\phi/\partial y$ at the same horizontal lattice position is caused by the high-order effects other than the singularity and can be explained by the dipole model. Denoting $i' = i - 1.5 = x$, and $j' = j - (H/2 + 1.5) = y - H/2$, Eq. (25) can be expressed as

$$\frac{\partial\phi_{\text{ex}}}{\partial x} \sim \frac{1}{\pi}\frac{j'}{i'^2 + j'^2} - 1.0471\frac{j'}{H^2}, \tag{26a}$$

$$\frac{\partial\phi_{\text{ex}}}{\partial y} \sim -\frac{1}{\pi}\frac{i'}{i'^2 + j'^2} + \frac{1}{H} - 1.0471\frac{i}{H^2}. \tag{26b}$$

The first terms on the RHS of Eq. (26) are independent of H on the lattice scale near $(i', j') = (0,0)$. For $\partial\phi_{\text{ex}}/\partial x$, the next term is of $O(H^{-2})$; hence the spread caused by the change in H is rather small. For $\partial\phi_{\text{ex}}/\partial y$, the next term is of $O(H^{-1})$ and is independent of i' and j'; hence the spread caused by the change in H is the same as shown in Fig. 6(b). Equation (26) predicts $\partial\phi_{\text{LBE}}/\partial x$ and $\partial\phi_{\text{LBE}}/\partial y$ shown in Fig. 6 well except at $(i', j') = (0.5, 0.5)$, where the LBE results overpredict the exact solution by about 15% in magnitude. For $f = f_{\text{parab}}(\eta)$ and $f_{\text{sine}}(\eta)$ the same is observed on the lattice scale for the leading order behavior; the spread is slightly different from that for $f = f_{\text{linear}}(\eta)$ due to the difference in the details of the smooth portion of $f(\eta)$; hence they are omitted for brevity.

Figure 7(a) compares $\partial\phi/\partial y$ values from the exact solution, the dipole model, and the LBE solution for $H = 64$ along

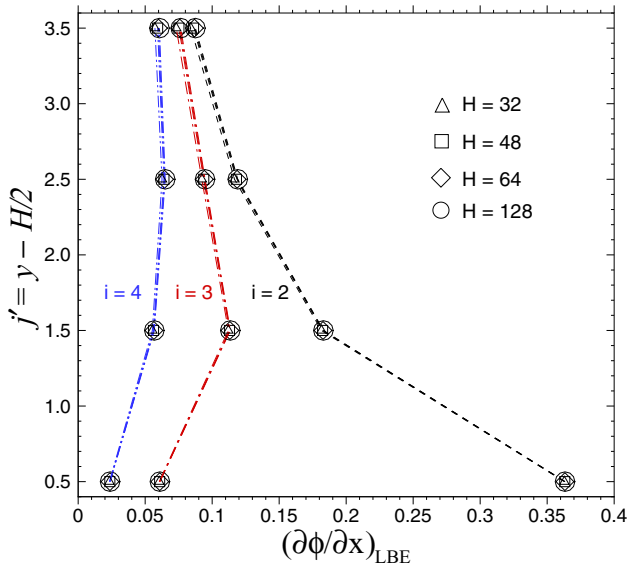

(a)

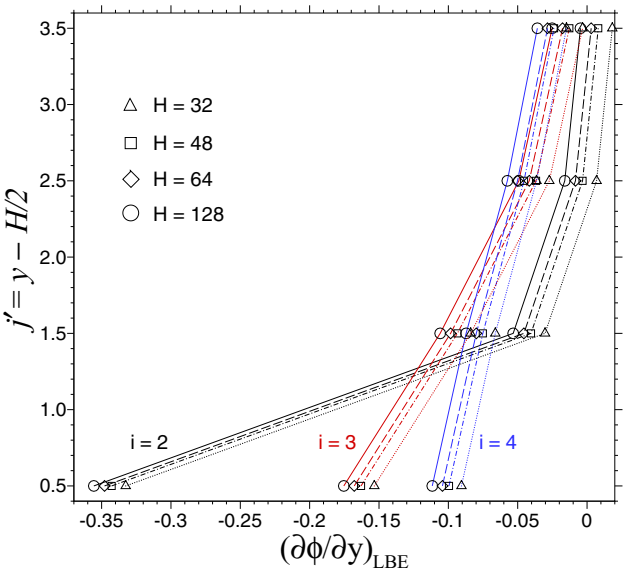

(b)

FIG. 6. Comparison of LBE results for the interior derivatives of (a) $\partial\phi/\partial x$ and (b) $\partial\phi/\partial y$ for different resolutions at $H = 32$, 48, 64, and 128, along the vertical lines at $i = 2$, 3, and 4 ("i" denotes the lattice nodes along the x direction, with the left wall placed halfway between $i = 1$ and $i = 2$, see Fig. 2), with $f_{\text{linear}}(\eta)$ on the left wall.

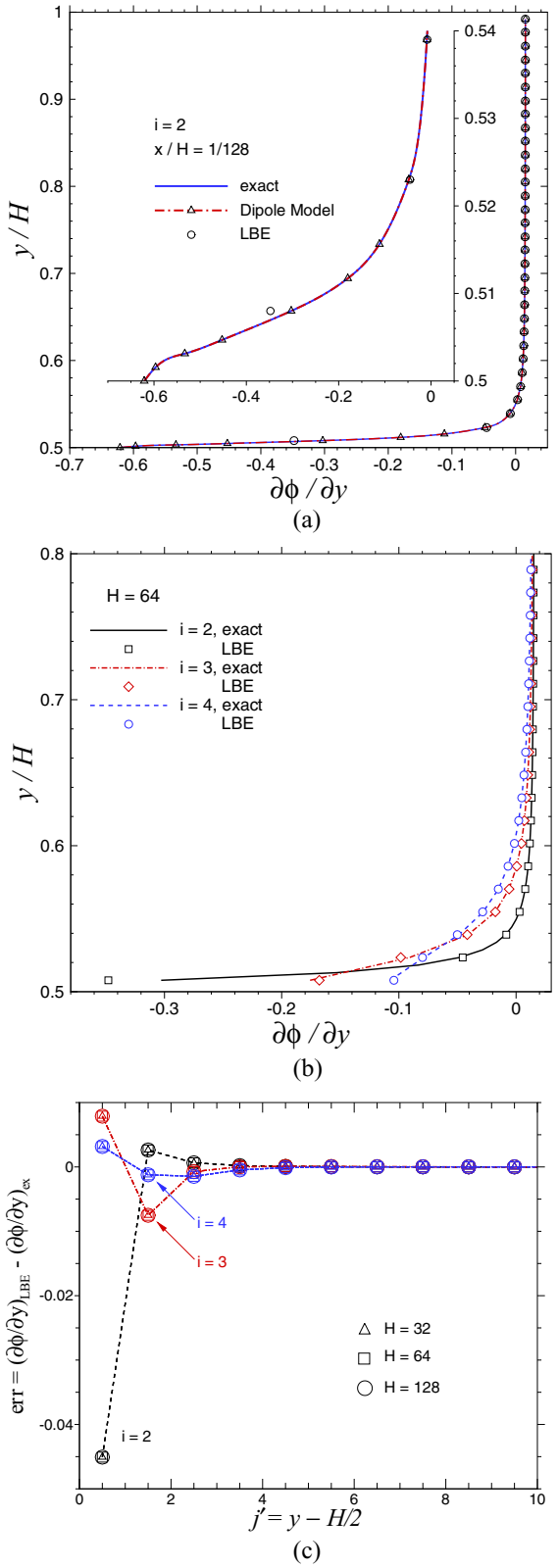

FIG. 7. (a) Comparison between the exact solution, the dipole model, and the LBE solution for $\partial\phi/\partial y$ along the vertical line at $i = 2$. (b) Comparison of $\partial\phi/\partial y$ near the left wall at $i = 2$, 3, and 4. (c) The absolute errors of err $= (\partial\phi/\partial y)_{\rm LBE} - (\partial\phi/\partial y)_{\rm ex}$ along the vertical lines near the left wall for different grid resolutions, with $f_{\rm linear}(\eta)$ on the left wall.

the entire upper half of the vertical line at $i = 2$ ($i' = 0.5$ or $x/H = 1/128$). Again, the dipole model captures the behavior of the singularity very nicely near $\eta = y/H = 0.5$. At $j' = 0.5$, the LBE solution has about 15% error due to the influence of the singularity as discussed in the preceding paragraph; this error is more clearly seen in the inset as indicated by the first open circle (LBE solution) away from the horizontal axis at $y/H = 0.5078$. It is emphasized that errors from the two lattice points, $(x/H, y/H) = [1/(2H), 0.5 \pm 1/(2H)]$ or $(i', j') = (0.5, \pm 0.5)$ on the lattice scale, are the biggest source of the error in the overall interior derivatives of the LBE solutions. Figure 7(b) compares $\partial\phi/\partial y$ values between the exact and LBE solutions at $i = 2$, 3, and 4, corresponding to $x/H = 1/128$, $3/128$, and $5/128$. The agreement becomes much better away from $i = 2$. Figure 7(c) shows the absolute errors in $\partial\phi/\partial y$, defined as err $= (\partial\phi/\partial y)_{\rm LBE} - (\partial\phi/\partial y)_{\rm ex}$, as a function of lattice node position $j' = y - H/2$ along the same vertical lines ($i = 2$, 3, and 4) near the left wall for $H = 32$, 64, and 128. Clearly the largest absolute error occurs at the lattice nodes closest to the discontinuity. Since both the LBE and exact solutions for the derivatives behave the same on the lattice scale, the errors of the LBE solutions remain invariant of the resolution H near the singularity. The implication of this behavior will be further discussed in the error analysis in later paragraphs. To further elucidate the behavior of the LBE errors near the discontinuity, the results from the three types of discontinuous boundary conditions, Eqs. (19a)–(19c), are compared. Figures 8(a) and 8(b) show the local relative errors for $\partial\phi/\partial x$ [R.E. $= {\rm err}/(\partial\phi/\partial x)_{\rm ex}$] and the normalized errors for $\partial\phi/\partial y$ (N.E. $= \frac{\rm err}{|\partial\phi/\partial y|_{\rm LBE,max}}$) along the vertical line at $i = 2$ for different resolution for all three cases. The normalized error, instead of the relative error, is used for $\partial\phi/\partial y$ since its exact solution at $i = 2$ goes through a zero between $y = H/2$ and $y = H$ and is thus inappropriate to be used in the denominator. On the other hand, $|\partial\phi/\partial y|_{\rm LBE,max}$ is an appropriate L_1 norm of the function based on the LBE solution. Figures 8(a) and 8(b) also show that the local errors for the interior derivatives behave the same for three different discontinuous boundary profiles. It is thus appropriate to conclude that the local error behavior for the derivatives shown in Figs. 8(a) and 8(b) is universally applicable for a unity jump in the Dirichlet boundary condition for conduction or diffusion problems governed by the Laplace equation.

In order to understand how the discontinuity affects the accuracy of the macroscopic quantities in the LBE computation, it is vital to examine the error behavior of the individual microscopic distribution functions, especially near the discontinuity. Figures 9(a)–9(e) shows the respective profiles of g_α ($\alpha = 0$–4) along the vertical line at $i = 2$ from both the asymptotic and LBE solutions for the linear case, where the asymptotic values are obtained from Eq. (16) in which $\phi^{(0)}$ is replaced by $\phi_{\rm ex}$. It is clear that $g_{0\_\rm LBE}$ matches well with its asymptotic value throughout the domain, while the other components all have much larger discrepancies near the discontinuity at $j' = 0.5$. This comparison is further illustrated by the errors $\gamma_\alpha = g_{\alpha\_\rm LBE} - g_{\alpha\_\rm asymptotic}$, in Fig. 10(a). Based on the results in Fig. 10(a), Fig. 10(b) also shows the absolute errors for the macroscopic ϕ value

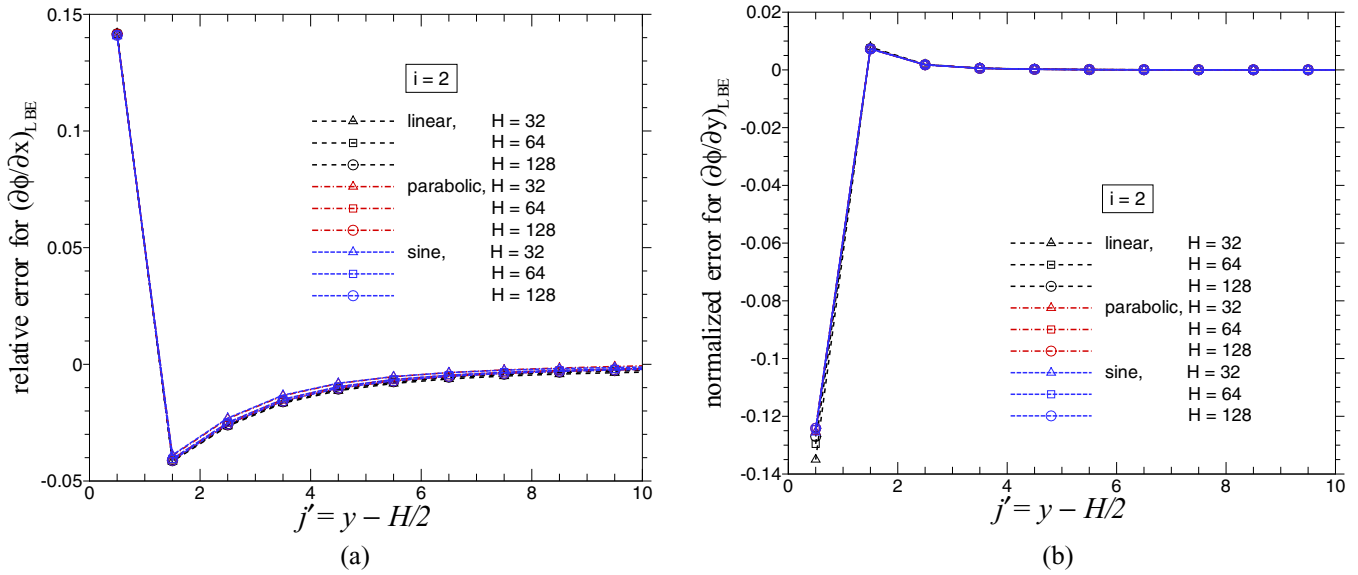

FIG. 8. (a) Relative errors for $\partial\phi/\partial x$ and (b) normalized errors for $\partial\phi/\partial y$ along the vertical line at $i = 2$ at different grid resolution for the three types of discontinuous Dirichlet conditions on the left wall.

and its derivatives following Eq. (17) [here $E_\phi = \sum_{\alpha=0}^{4} \gamma_\alpha$, $E_{\partial\phi/\partial x} = \kappa(\gamma_1 - \gamma_2)$, and $E_{\partial\phi/\partial y} = \kappa(\gamma_3 - \gamma_4)$]. Clearly the large errors in the derivatives are attributed to the difference between the errors of the distribution functions; while for the macroscopic ϕ value, the dominating errors in γ_α ($\alpha = 1$–4) cancel each other out. This explains well that while the interior derivatives have zeroth-order accuracy with resolution, the error for the interior distribution of ϕ does decrease with resolution. It should also be noted that the errors for $\partial\phi/\partial x$ and $\partial\phi/\partial y$ in Fig. 10(b) obtained from the comparison with the asymptotic microscopic distribution functions match very well with the errors in Figs. 7(c), 8(a), and 8(b), where the solutions are directly compared to the exact macroscopic quantities. Furthermore, the same error behavior in Figs. 10(a)

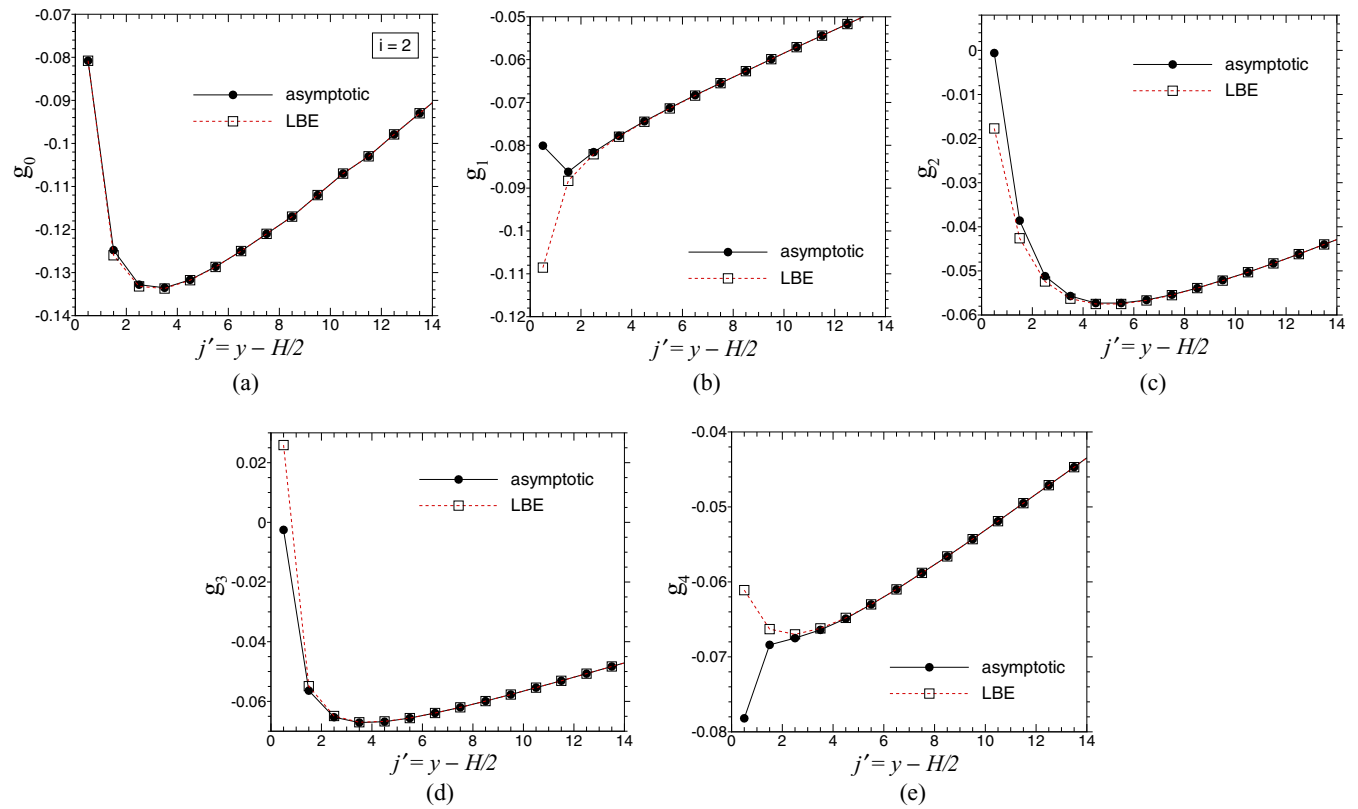

FIG. 9. Profiles of the microscopic distribution functions (a) g_0, (b) g_1, (c) g_2, (d) g_3, and (e) g_4 along the vertical line at $i = 2$, for both the asymptotic and LBE solutions for the linear case.

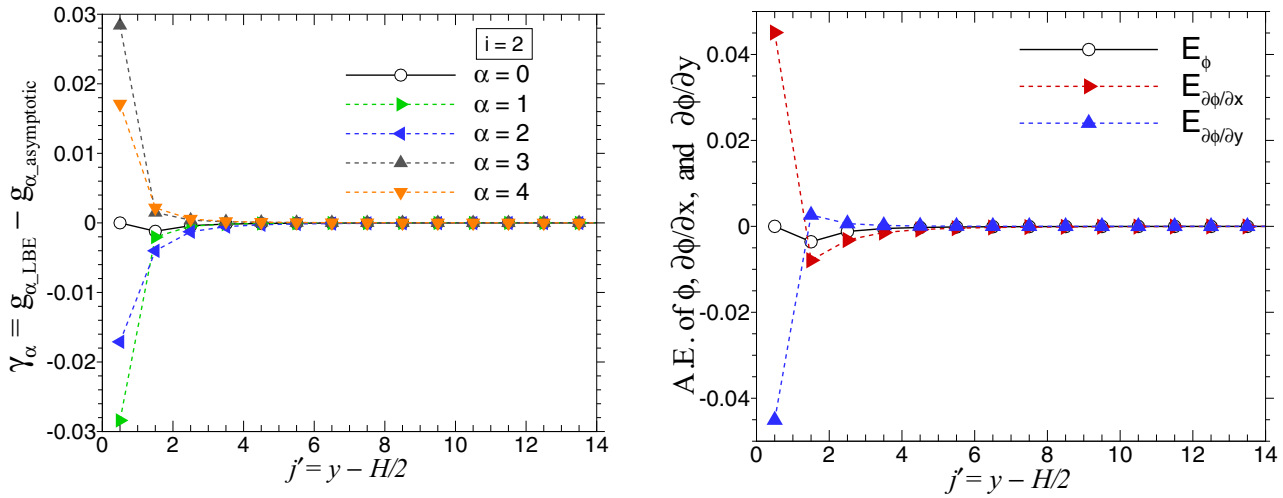

FIG. 10. (a) Absolute errors γ_α for the microscopic distribution functions g_{α_LBE} compared to the corresponding asymptotic values $g_{\alpha\_\mathrm{asymptotic}}$ in Fig. 9, and (b) the absolute errors for the macroscopic values $E_\phi = \sum_{\alpha=0}^{4} \gamma_\alpha$, $E_{\partial\phi/\partial x} = \kappa(\gamma_1 - \gamma_2)$, and $E_{\partial\phi/\partial y} = \kappa(\gamma_3 - \gamma_4)$, using the data in (a).

and 10(b) is observed for the other two cases with piecewise parabolic and sine Dirichlet conditions, confirming that the LBE solution near the discontinuity is controlled by the local solution dominated by the jump in the boundary condition.

Fixed relaxation time coefficients $\tau_D = 0.75$ and $\tau_p = 1.0$ [thus $\Lambda = (\tau_D - 0.5)(\tau_p - 0.5) = 1/8$] have been used in the foregoing discussion. The effect of Λ on the accuracy of the interior derivative is examined next. Figure 11 shows the variation of the absolute errors for $(\partial\phi/\partial x)_{\mathrm{LBE}}$ and $(\partial\phi/\partial y)_{\mathrm{LBE}}$ with Λ at the interior lattice node $P(i' = j' = 0.5)$ next to the singularity point. The variation of Λ is realized by changing τ_D while keeping $\tau_p = 1$. For each Λ, the two derivatives computed have the same error magnitude and with opposite signs. Both show monotonic behavior and a sign change. This indicates that for certain Λ values, the maximum error magnitude for the derivatives is not at P, the closest lattice node near the singularity. The present computation shows that for these cases (e.g., $\Lambda = 0.0005$, 0.0025, 0.25, 0.375) the maximum error magnitudes for $(\partial\phi/\partial x)_{\mathrm{LBE}}$ and $(\partial\phi/\partial y)_{\mathrm{LBE}}$ are found at the lattice nodes next to P on the right and at the top, respectively. For all other Λ values examined, the maximum errors are found at P. It should be noted that for all Λ values tested, the overall derivative error in the interior field, which represents the convergence orders, do not change with grid resolution. This will be further studied in the following section.

d. Order-of-accuracy of LBE solutions. To assess the numerical accuracy of the LBE results, the following relative L_2-norm errors are defined following [17]:

$$E_2 = \left[\sum_{\text{interior nodes}} (\phi_{\mathrm{LBE}} - \phi_{\mathrm{ex}})^2 \Big/ \sum_{\text{interior nodes}} \phi_{\mathrm{ex}}^2 \right]^{1/2}, \tag{27}$$

$$E_{2\_\partial\phi/\partial x} = \left[\sum_{\text{interior nodes}} \left(\frac{\partial\phi}{\partial x}\bigg|_{\mathrm{LBE}} - \frac{\partial\phi}{\partial x}\bigg|_{\mathrm{ex}} \right)^2 \Big/ \sum_{\text{interior nodes}} \left(\frac{\partial\phi}{\partial x}\bigg|_{\mathrm{ex}} \right)^2 \right]^{1/2}, \tag{28a}$$

$$E_{2\_\partial\phi/\partial y} = \left[\sum_{\text{interior nodes}} \left(\frac{\partial\phi}{\partial y}\bigg|_{\mathrm{LBE}} - \frac{\partial\phi}{\partial y}\bigg|_{\mathrm{ex}} \right)^2 \Big/ \sum_{\text{interior nodes}} \left(\frac{\partial\phi}{\partial y}\bigg|_{\mathrm{ex}} \right)^2 \right]^{1/2}, \tag{28b}$$

$$E_{2\_\mathrm{qw}} = \left[\sum_{\text{boundarynodes}} \left(D\frac{\partial\phi}{\partial x}\bigg|_{\mathrm{LBE}} - D\frac{\partial\phi}{\partial x}\bigg|_{\mathrm{ex}} \right)^2 \Big/ \sum_{\text{boundarynodes}} \left(D\frac{\partial\phi}{\partial x}\bigg|_{\mathrm{ex}} \right)^2 \right]^{1/2}, \tag{29}$$

where the "interior nodes" denote the lattice nodes inside the block but not on the boundary walls, and the "boundary nodes" in Eq. (29) refer to those on each straight section of the boundary walls.

We first computed the L_2-norm errors in Eqs. (27)–(29) by choosing different τ_D and τ_p values while maintaining the same value of $\Lambda = (\tau_D - 0.5)(\tau_p - 0.5)$. It is verified that for each Λ value, the different τ_D and τ_p combinations

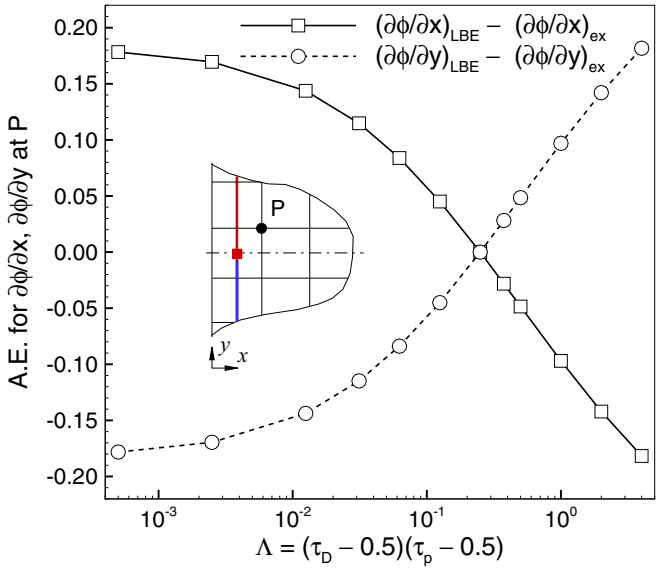

FIG. 11. Variation of the absolute errors for $(\partial\phi/\partial x)_{\mathrm{LBE}}$ and $(\partial\phi/\partial y)_{\mathrm{LBE}}$ with $\Lambda = (\tau_D - 0.5)(\tau_p - 0.5)$ at the interior lattice node P next to the singularity point.

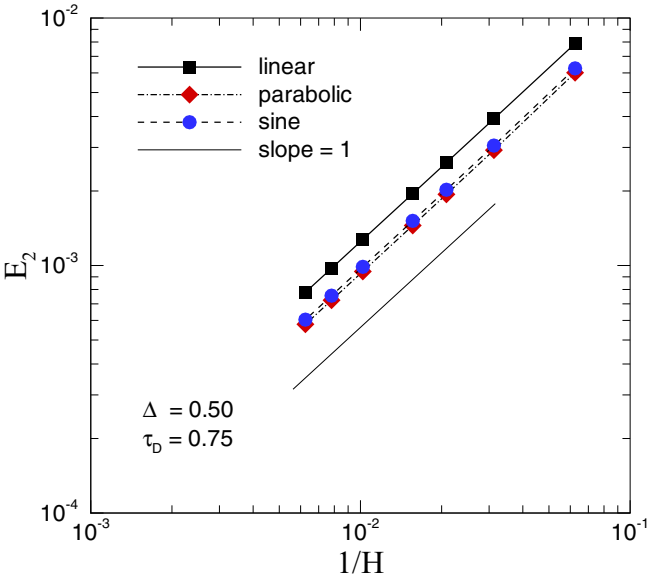

FIG. 13. Relative L_2-norm error E_2 of the interior distribution of ϕ versus the grid resolution $1/H$ for steady diffusion in the square block with discontinuous Dirichlet boundary conditions and the discontinuity point placed at the center of the unit lattice, i.e., $\Delta_d = \Delta_w = \Delta = 0.5$ (see Fig. 2).

result in almost exactly the same L_2-norm errors for this pure diffusion problem (as shown later in Fig. 30, the errors are determined by Λ also for convection-diffusion problems with both continuous and discontinuous boundary conditions). The variations of the L_2-norm errors with Λ is thus examined and the results for the case with $f_{\mathrm{linear}}(\eta)$ are shown in Fig. 12 with $\tau_p = 1$. The comparison between Figs. 12(a) and 12(b) clearly shows that the errors are much less when the discontinuity point is placed at the center of the lattice with the symmetry preserved. An optimal Λ value near $1/8$ is seen in Fig. 12(a) and $\Lambda = 1/8$ is also a good choice for $\Delta_d = 0.25$ in Fig. 12(b). Thus the choice of $\Lambda = 1/8$ is recommended and used in most cases shown below. For $\Delta = 0.5$ in Fig. 10(a), the dependence of E_2 on Λ can be well approximated by a power function $E_2 \sim \{^{-0.093\sqrt{\Lambda}+0.038,\ \Lambda\leqslant 1/8,}_{0.095\sqrt{\Lambda}+0.034,\ \Lambda\geqslant 1/8.}$ This leading-order power in $\sqrt{\Lambda}$ is consistent with that reported in [36].

Figures 13 and 14 show the respective relative errors defined in Eqs. (27)–(28) versus the grid resolution $1/H$ at $\Delta_d = \Delta_w = \Delta = 0.5$ and $\tau_D = 0.75$. Due to the tangential discontinuity of the Dirichlet boundary conditions at $x = 0$, the order of accuracy of the interior field is reduced to first order, as shown in Fig. 13, and that of the interior derivatives to zeroth order, as shown in Fig. 14, for all three forms of $f(\eta)$. For the same H, the relative errors for all three cases are close in magnitude because the jump magnitudes of all three cases are equal to unity. The zeroth-order accuracy for the interior derivatives

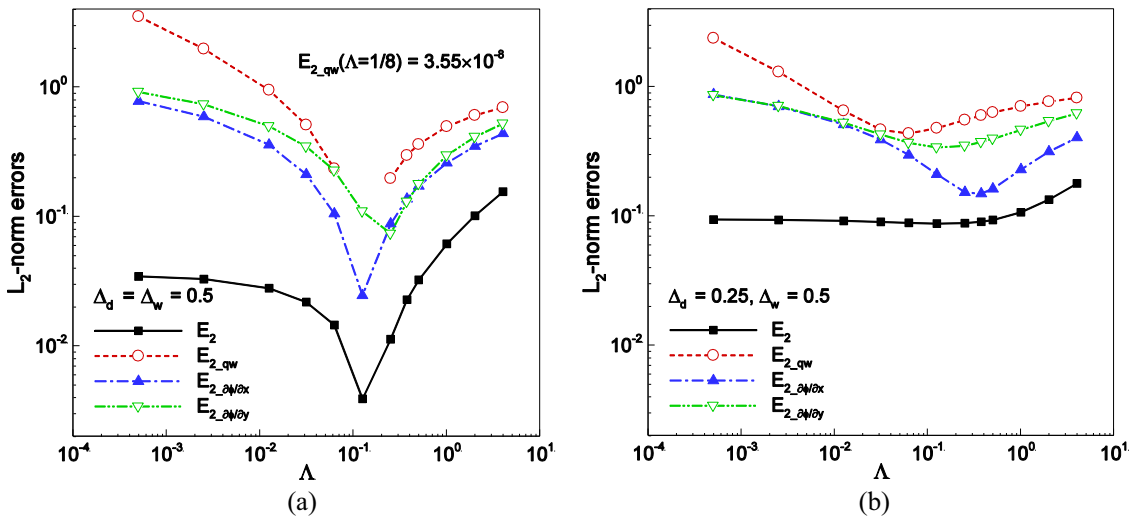

FIG. 12. Relative L_2-norm errors versus $\Lambda = (\tau_D - 0.5)(\tau_p - 0.5)$ for steady diffusion in the square block ($H = 32$) with a discontinuous boundary condition $f_{\mathrm{linear}}(\eta)$ on the left wall at (a) $\Delta_d = \Delta_w = 0.5$ and (b) $\Delta_d = 0.25$, $\Delta_w = 0.5$.

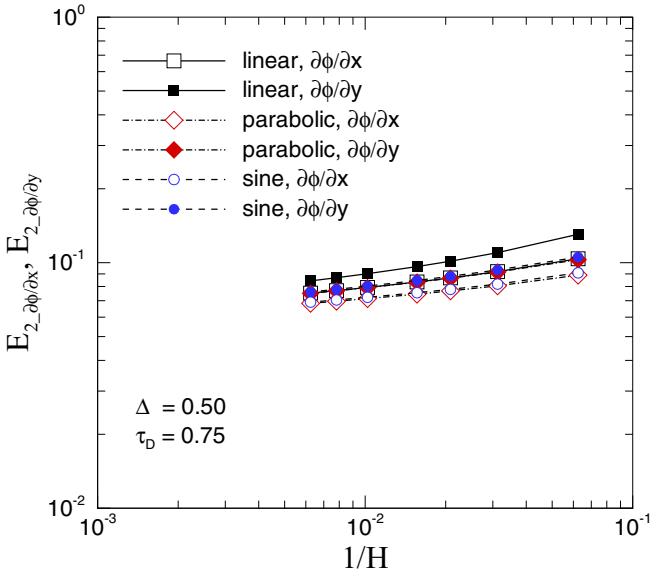

FIG. 14. Relative L_2-norm errors $E_{2\_\partial\phi/\partial x}$ and $E_{2\_\partial\phi/\partial y}$ of the interior derivatives versus $1/H$ for steady diffusion in the square block with discontinuous Dirichlet boundary conditions ($\Delta_d = \Delta_w = \Delta = 0.5$).

can be explained by the results shown in Figs. 5–8. As the resolution increases on the lattice scale, the absolute errors on the lattice nodes near the discontinuity point remain invariant with H. Since the errors are much higher near the discontinuity than those far away from the discontinuity, both the numerators and denominators in Eqs. (28a) and (28b) change very slowly with H, resulting in a zeroth-order accuracy.

Figure 15(a) shows the boundary flux errors at $x = 0$, $x = L = H$, and $y = H$, respectively [$\partial\phi/\partial x$ is changed to $\partial\phi/\partial y$ in Eq. (29) for $y = H$], when the discontinuous $f = f_{\text{linear}}(\eta)$ is used at $x = 0$ and $\Delta_d = \Delta_w = \Delta = 0.5$ is maintained. The most striking feature is the exceptionally small relative error in the normal flux at $x = 0$ where the discontinuous linear profile of $\phi(0, y)$ is imposed; and quadruple precision was used in the evaluation of wall normal derivative mainly for this case to ensure that the round-off error in the exact solution does not exceed the exceptionally small numerical error for wall normal flux. However, the relative errors on the right and top walls, where $\phi_w = 0$ are imposed, are not so small; they show second-order convergence behavior and have magnitudes in line with those observed in earlier studies [17–20] for wall flux. The exceptionally small flux error at $x = 0$ also prompted the use of the discontinuous parabolic and sine profiles $f_{\text{parab}}(\eta)$ and $f_{\text{sine}}(\eta)$ for $f(\eta)$ in this study as it is believed that the small flux error may be caused by the use of the linear or zeroth-order $f(\eta)$ at $x = 0$. Figure 15(b) shows the relative flux errors on two walls, $x = 0$ and $x = L$, when $f(\eta) = f_{\text{parab}}(\eta)$ and $f_{\text{sine}}(\eta)$ at $x = 0$ are enforced. The second-order convergence is observed and the magnitude of the flux errors is indeed in line with previous observations [17–20]. Another test was also conducted by setting $\phi(\xi = 1, \eta) = 0.5\sin(\pi\eta)$ in addition to keeping $\phi(0, \eta) = f_{\text{linear}}(\eta)$ and $\phi(\xi, \eta = 0) = f(x, \eta = 1) = 0$. Not surprisingly, the L_2-norm error E_{2_qw} for the wall flux at $x = 0$ becomes comparable with E_{2_qw} shown in Fig. 15(b). This suggests that the exceptionally small magnitude of the flux error at $x = 0$ for the discontinuous linear $f_{\text{linear}}(\eta)$ is indeed an exception.

To elucidate the effect of the location of the tangential-type boundary condition discontinuity on the accuracy of the LBE results, Figs. 16–18 show the relative L_2-norm errors defined in Eqs. (27)–(29), respectively, versus $1/H$ for three cases with $(\Delta_d, \Delta_w) = (0.5, 0.25)$, $(0.25, 0.5)$, and $(0.25, 0.25)$ when $f(\eta) = f_{\text{linear}}(\eta)$ is used at $x = 0$. Scheme 2 in Eq. (10b) is applied for all the Dirichlet boundary conditions. Other combinations with $\Delta_d = 0.75$, 0.01, 0.99 and $\Delta_w = 0.75$, 0.01, 0.99 are also examined and they show the same convergence behavior as in Figs. 16–18 and are not shown for brevity. When the discontinuity is placed away from the lattice center, the accuracy of the interior ϕ values

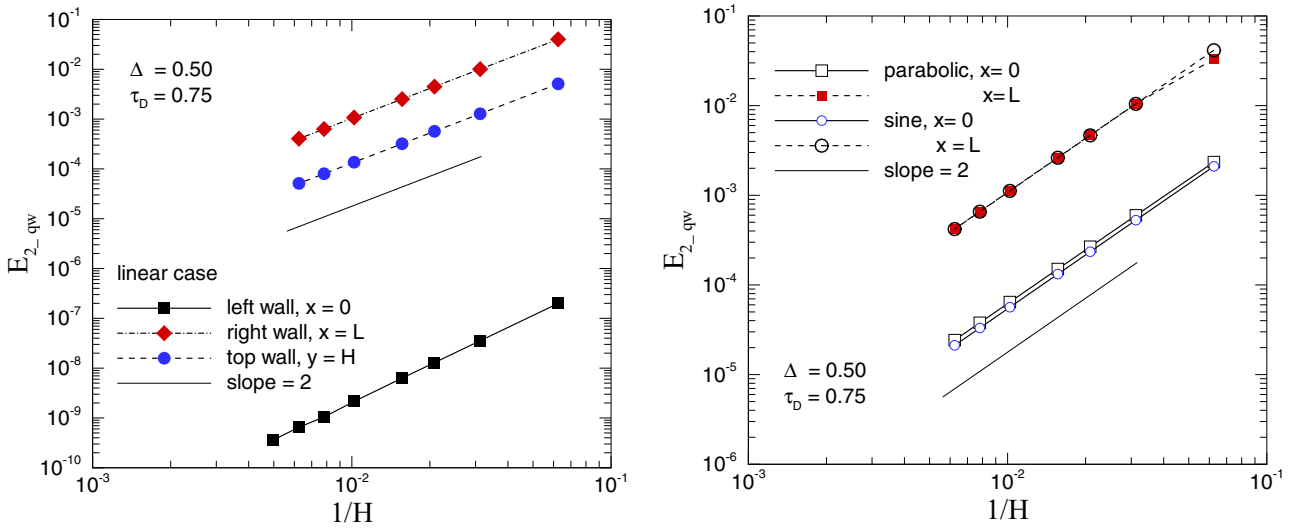

FIG. 15. Relative L_2-norm error E_{2_qw} of the boundary flux versus $1/H$ for steady diffusion in the square block with discontinuous boundary conditions (a) $f_{\text{linear}}(\eta)$ and (b) $f_{\text{parab}}(\eta)$ and $f_{\text{sine}}(\eta)$ on the left wall ($\Delta_d = \Delta_w = \Delta = 0.5$).

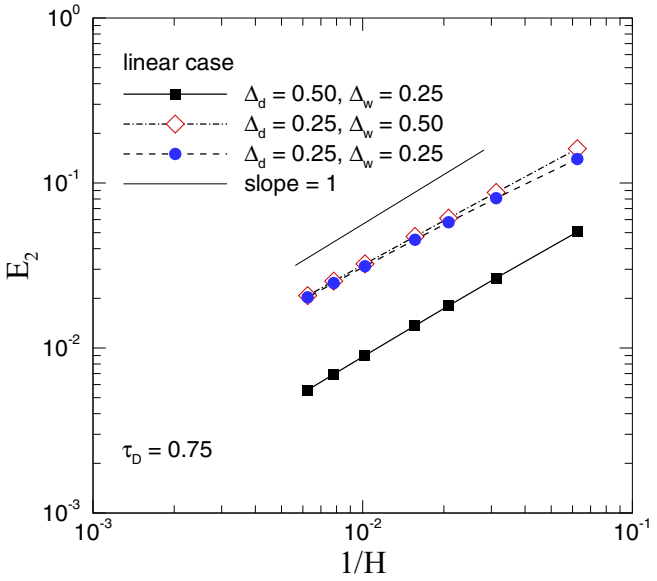

FIG. 16. Relative L_2-norm error E_2 of the interior distribution of ϕ versus $1/H$ for steady diffusion in the square block with $f_{\text{linear}}(\eta)$ on the left wall and the discontinuity point off the lattice center.

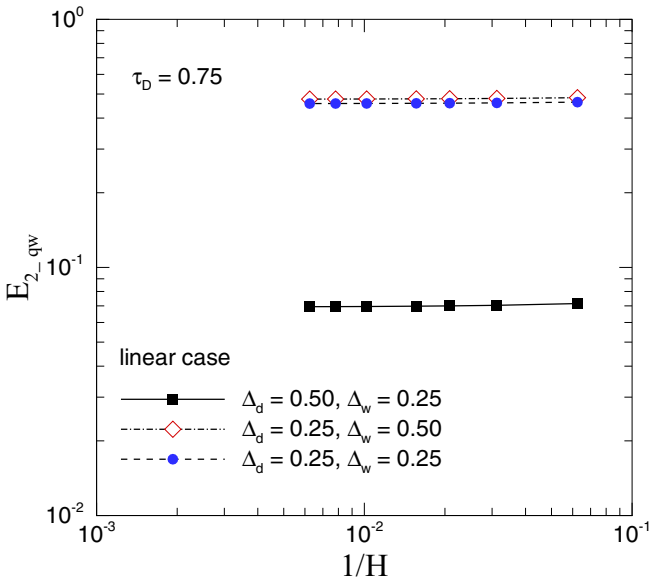

FIG. 18. Relative L_2-norm error E_{2_qw} of the boundary flux versus $1/H$ for steady diffusion in the square block with $f_{\text{linear}}(\eta)$ on the left wall and the discontinuity point off the lattice center.

remains first order; however the relative errors in Fig. 16 are substantially larger than those in Fig. 13. The loss of the geometric symmetry of the lattices relative to the discontinuity position results in the disappearance of the antisymmetry of the ϕ_{LBE} values on the two sides of the discontinuity relative to the averaged discontinuous value $\frac{1}{2}[\phi(0,\eta = 0.5^-) + \phi(0,\eta = 0.5^+)]$. Hence the error near the discontinuity is larger than the case when $(\Delta_d, \Delta_w) = (0.5, 0.5)$. For the interior derivatives, the accuracy is again of zeroth order with larger magnitude, as one can observe by comparing Fig. 17 with Fig. 14. Most

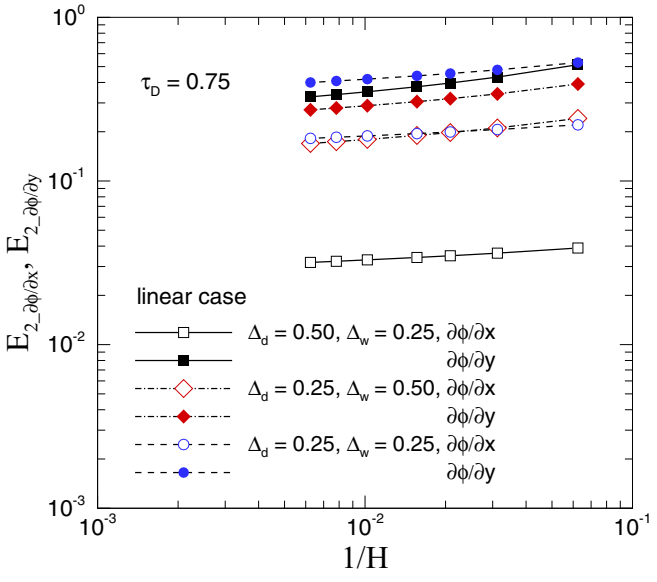

FIG. 17. Relative L_2-norm errors $E_{2\_\partial\phi/\partial x}$ and $E_{2\_\partial\phi/\partial y}$ of the interior derivatives versus $1/H$ for steady diffusion in the square block with $f_{\text{linear}}(\eta)$ on the left wall and the discontinuity point off the lattice center.

strikingly, the error for the wall flux changes from second order (Fig. 15) to zeroth order (Fig. 18) with the loss of the geometric symmetry. Thus whenever possible the discontinuity point should be placed at the center of the lattice in order to reduce the LBE errors for the quantities of interest.

2. *Discontinuous Neumann boundary condition*

For the Neumann problem, the boundary condition on the left wall is imposed as

$$\Phi_n = -D\frac{\partial\phi}{\partial x}\bigg|_{x=0,y} = -\frac{D}{H}\frac{\partial\phi}{\partial\xi}\bigg|_{\xi=0,\eta} = -\frac{D}{H}f(\eta). \quad (30)$$

The same discontinuous functions $f(\eta)$ given in Eqs. (21a)–(21c) are used in Eq. (30) for consistency. Similar to Eq. (22), the exact solution ϕ for the Neumann problem can be expressed as

$$\phi_{\text{ex}}(\xi,\eta) = \frac{2}{\pi}\sum_{n=1}^{M}\frac{b_n}{n}\sin(n\pi\eta)\frac{\sinh[n\pi(\xi - L/H)]}{\cosh(-n\pi L/H)} + \frac{2}{\pi}\sum_{n=M+1}^{N_\infty}\frac{b_n}{n}\sin(n\pi\eta)[e^{n\pi(\xi-2L/H)} - e^{-n\pi\xi}], \quad (31)$$

where the Fourier coefficients b_n are the same as given in Eq. (20b). For the interior derivatives, the exact values can be obtained from Eq. (31) through direct differentiation. For Neumann problems $\phi_{\text{ex}}(\xi = 0, \eta)$ is calculated using Eq. (31) in order to assess the accuracy of the computed LBE boundary value Φ_d using Eq. (14).

To assess the accuracy of the LBE solution for Φ_d, the relative L_2-norm error for Φ_d at $x = 0$ is defined in the

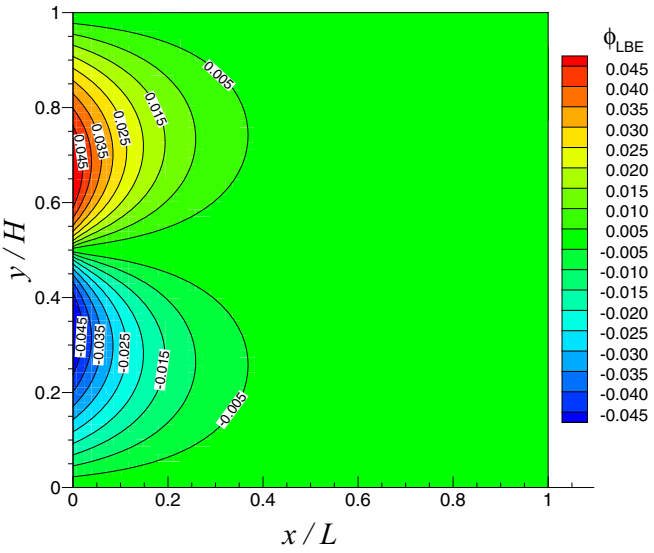

FIG. 19. Contours of ϕ_{LBE} at $H = L = 64$ with a piecewise linear discontinuous Neumann condition on the left wall ($\Delta_d = \Delta_w = \Delta = 0.5$).

following in addition to those defined in Eqs. (27) and (28):

$$E_{2\_\mathrm{tw}} = \left[\sum_{\text{boundary nodes}} (\Phi_{d,\mathrm{LBE}} - \phi_{\mathrm{ex}})^2 \Big/ \sum_{\text{boundary nodes}} \phi_{\mathrm{ex}}^2 \right]^{1/2}, \tag{32}$$

where the "boundary nodes" refer to those on the left boundary wall.

Similar to the Dirichlet problem, $\Delta_d = \Delta_w = \Delta = 0.5$ is considered first for the LBE results in Figs. 19–22. Figure 19 shows the contours of ϕ_{LBE} for $f = f_{\mathrm{linear}}(\eta)$ with $H = 64$;

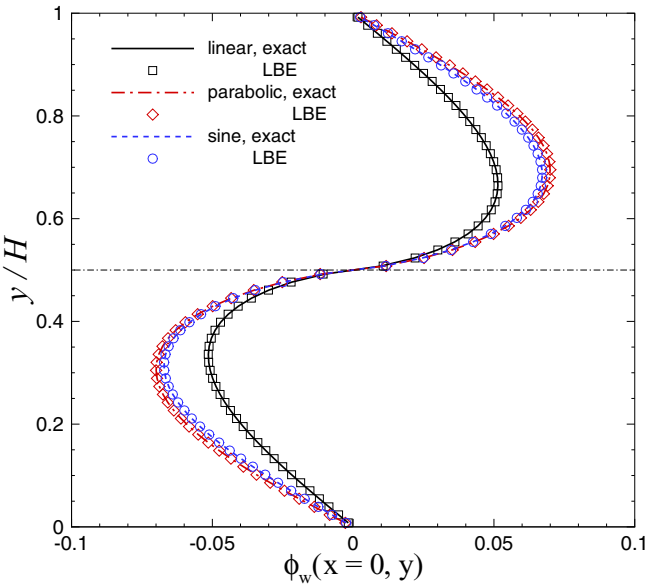

FIG. 20. Profiles of $\phi_w(x = 0, y)$ on the left wall at $H = 64$, $\tau_D = 0.75$, and $D = 1/12$ with discontinuous Neumann conditions on the left wall.

those for $f = f_{\mathrm{parab}}(\eta)$ and $f_{\mathrm{sine}}(\eta)$ are very similar and are not shown. Figure 20 compares the profiles of $\phi_{\mathrm{LBE}}(x = 0, y)$ evaluated using Eq. (14) with the exact solutions for all three forms of $f(\eta)$. Excellent agreement is observed between the LBE and exact solutions. Clearly $\phi(x = 0, y)$ is continuous in the vicinity of $y = H/2$ where a discontinuity of boundary flux is present. Figures 21(a) and 21(b) show the contours for the derivatives $\partial\phi/\partial x$ and $\partial\phi/\partial y$ based on the LBE solution for $H = 64$. In the absence of a singularity, the magnitude for each derivative is much smaller than that for the Dirichlet problem. Figure 22 shows the absolute errors $\mathrm{err} = (\partial\phi/\partial y)_{\mathrm{LBE}} - (\partial\phi/\partial y)_{\mathrm{ex}}$ along the vertical lines near the left wall for $H = 32$, 64, and 128. The magnitude of the absolute errors for the derivatives decreases with the improvement of grid resolution instead of remaining invariant with resolution in the Dirichlet problem.

The results for E_2, E_{2_tw}, $E_{2\_\partial\phi/\partial x}$, and $E_{2\_\partial\phi/\partial y}$ defined in Eqs. (27), (32), (28a) and (28b) versus the grid resolution for all three forms of $f(\eta)$ at $x = 0$ for $\Delta_d = \Delta_w = \Delta = 0.5$ are shown in Figs. 23–25, respectively. For different Δ_d and Δ_w values, $f_{\mathrm{linear}}(\eta)$ is selected and the corresponding results are shown in Figs. 26–28 for $(\Delta_d, \Delta_w) = (0.5, 0.25)$, (0.25, 0.5), and (0.25, 0.25). Scheme 2 in Eq. (10b) is used for computing the boundary Φ_d values in Eq. (14). The results in Figs. 23, 24, 26, and 27 indicate that when the discontinuity point is placed halfway in the lattice along the tangential direction of the boundary, i.e., $\Delta_d = 0.5$, the LBE results are second-order accurate for interior ϕ field and superlinear (order ~1.5) for the boundary Φ_d values no matter what Δ_w values are used. When $\Delta_d \neq 0.5$, both the interior and boundary values become first-order accurate. The interior derivatives are first-order accurate for all cases as shown in Figs. 25 and 28. Other combinations of Δ_d and Δ_w values are also examined and the same patterns as in Figs. 23–28 are observed; thus they are not shown. Compared to the Dirichlet problem, the effect of the boundary condition discontinuity on the accuracy of the LBE results is less severe in general in the Neumann problem.

For both Dirichlet and Neumann problems, it is much preferred to place the discontinuity point at the lattice center with half lattice link fractions in both directions ($\Delta_d = \Delta_w = 0.5$). Such an arrangement could potentially improve the order of accuracy and/or reduce the magnitude of the errors.

B. Convection-diffusion in a channel

In this test, steady convection and diffusion of temperature or concentration in channel flow are considered. The geometric configuration and the lattice distributions are depicted in Fig. 29. Discontinuous Dirichlet or Neumann boundary conditions are imposed on the top and bottom walls, and periodic boundary conditions are assumed in the x direction for both ϕ and the distribution function g_α [17]. To obtain closed-form exact solutions, a plug flow is assumed following [17]. The governing CDE reads

$$U\frac{\partial\phi}{\partial x} = D\left(\frac{\partial^2\phi}{\partial x^2} + \frac{\partial^2\phi}{\partial y^2}\right), \tag{33}$$

where U is the constant velocity in the x direction, and the velocity in the y direction is zero. This thermal or mass

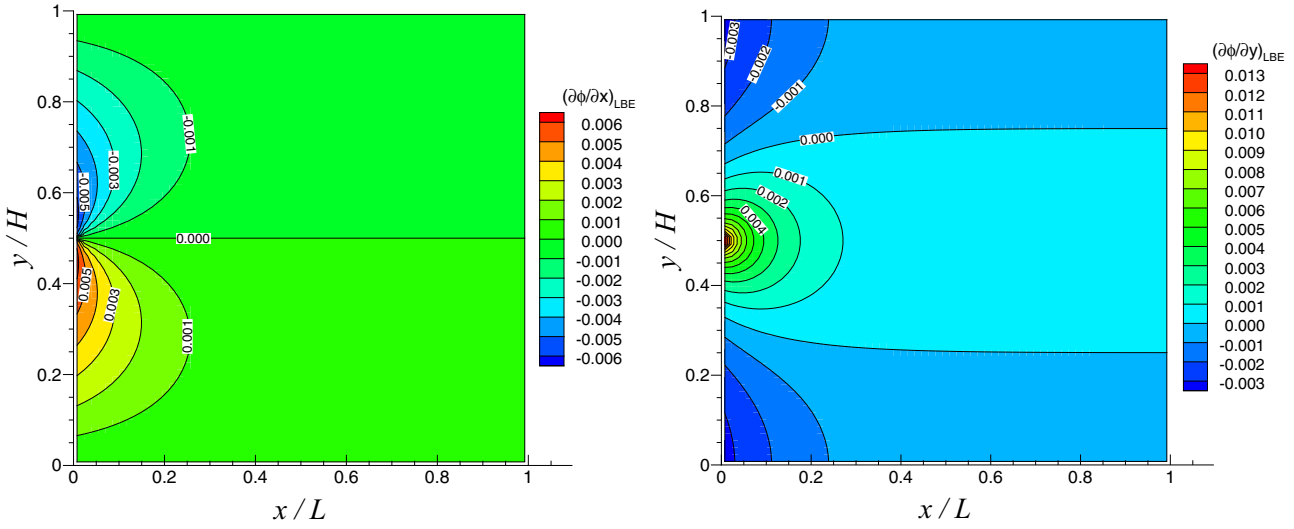

FIG. 21. Contours for interior derivatives (a) $\partial\phi/\partial x$ and (b) $\partial\phi/\partial y$ at $H = L = 64$ with a piecewise linear discontinuous Neumann condition on the left wall.

transport problem is characterized by the Péclet number defined as $\mathrm{Pe} = UH/D$.

1. Discontinuous Dirichlet boundary condition

As shown in Fig. 29, the tangential-type discontinuous Dirichlet boundary conditions are imposed as

$$\phi_w(y=0) = \phi_w(y=H) = F(x) = \begin{cases} 0.5, & 0 \leqslant x < L/4, \\ -0.5, & L/4 < x < 3L/4, \\ 0.5, & 3L/4 < x < L. \end{cases} \quad (34)$$

Using Fourier series expansion, $F(x)$ in Eq. (34) can be expressed as

$$F(x) = \frac{2}{\pi}\sum_{n=1}^{\infty}\frac{(-1)^{n+1}}{2n-1}\cos[(2n-1)2\pi\xi], \quad \xi = x/L. \quad (35)$$

Thus the exact solution for the scalar variable ϕ can be expressed using complex variables as

$$\phi_{\mathrm{ex}}(x,y) = \frac{2}{\pi}\mathrm{Re}\left[\sum_{n=1}^{\infty}\frac{(-1)^{n+1}}{2n-1}e^{i(2n-1)2\pi\xi}\frac{e^{\lambda_{2n-1}y}+e^{\lambda_{2n-1}(H-y)}}{e^{\lambda_{2n-1}H}+1}\right], \quad (36)$$

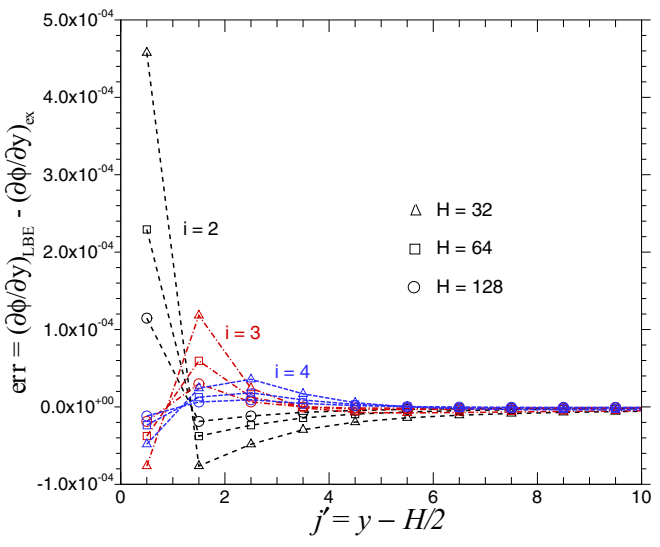

FIG. 22. Absolute errors of $\mathrm{err} = (\partial\phi/\partial y)_{\mathrm{LBE}} - (\partial\phi/\partial y)_{\mathrm{ex}}$ along the vertical lines near the left wall at $i = 2$, 3, and 4 for different grid resolutions, with a piecewise linear discontinuous Neumann condition on the left wall.

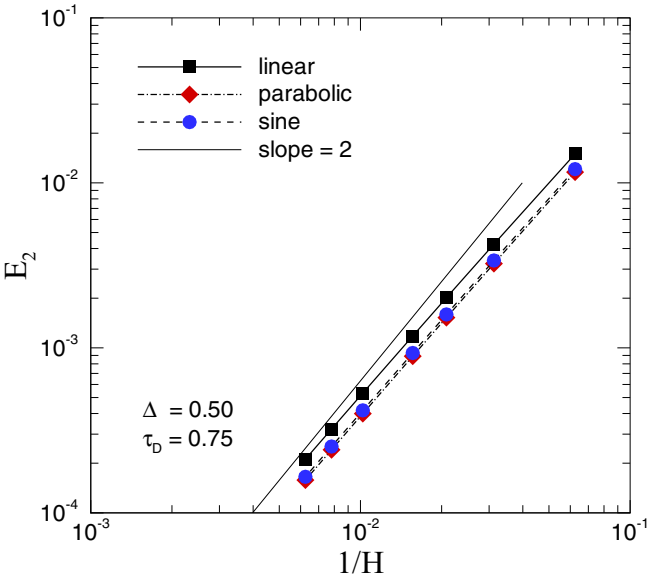

FIG. 23. Relative L_2-norm error E_2 of the interior ϕ values versus $1/H$ for steady diffusion in the square block with discontinuous Neumann boundary conditions ($\Delta_d = \Delta_w = \Delta = 0.5$).

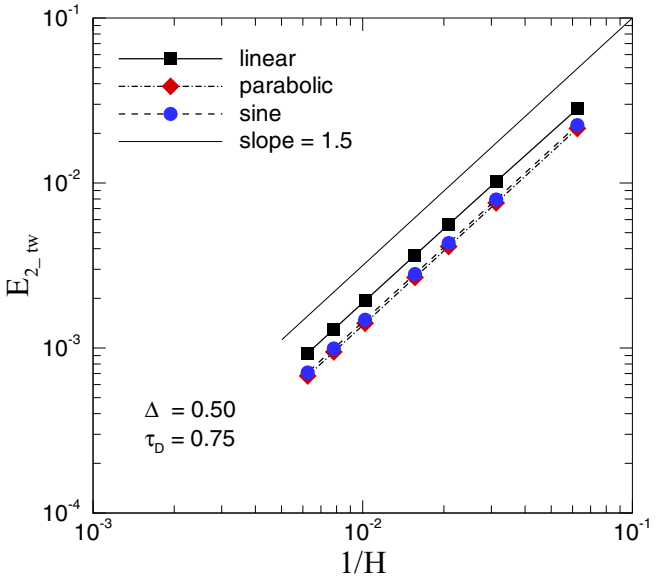

FIG. 24. Relative L_2-norm error E_{2_tw} of the boundary ϕ_w values versus $1/H$ for steady diffusion in the square block with discontinuous Neumann boundary conditions ($\Delta_d = \Delta_w = \Delta = 0.5$).

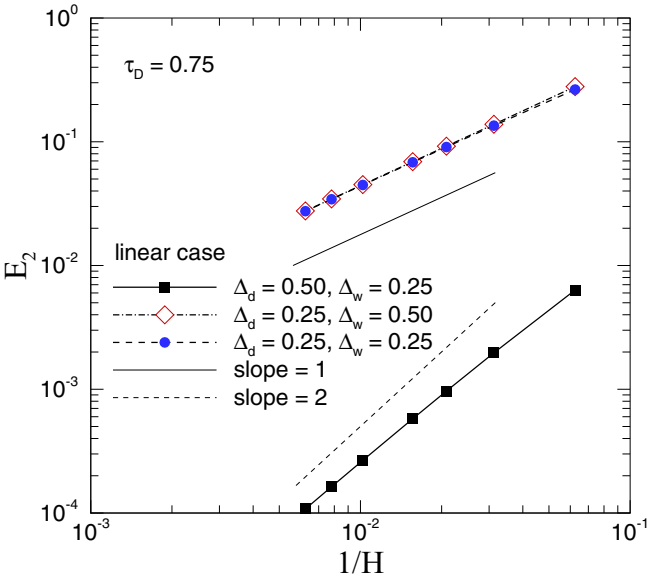

FIG. 26. Relative L_2-norm error E_2 of the interior ϕ values versus $1/H$ for steady diffusion in the square block with the Neumann condition $f_{\text{linear}}(\eta)$ on the left wall and the discontinuity point off the lattice center.

where "Re" means taking the real part of a complex number, and

$$\lambda_{2n-1} = \frac{(2n-1)2\pi}{L}\sqrt{1+\frac{iUL}{D(2n-1)2\pi}}.$$

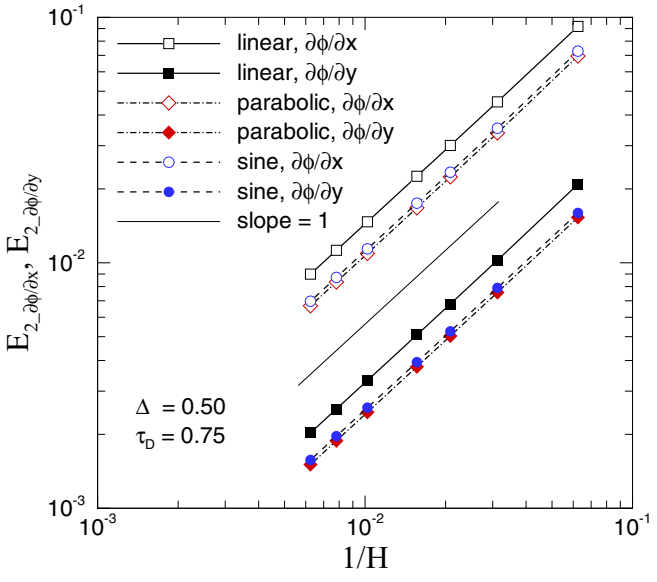

FIG. 25. Relative L_2-norm errors $E_{2\_\partial\phi/\partial x}$ and $E_{2\_\partial\phi/\partial y}$ of the interior derivatives versus $1/H$ for steady diffusion in the square block with discontinuous Neumann boundary conditions ($\Delta_d = \Delta_w = \Delta = 0.5$).

As discussed in the previous diffusion problem, the solution in Eq. (36) can be rearranged as

$$\phi_{\text{ex}}(x,y) = \frac{2}{\pi}\text{Re}\left\{\sum_{n=1}^{M}\frac{(-1)^{n+1}}{2n-1}e^{i(2n-1)2\pi\xi}\frac{e^{\lambda_{2n-1}y}+e^{\lambda_{2n-1}(H-y)}}{e^{\lambda_{2n-1}H}+1}\right.$$
$$+\sum_{n=M+1}^{N_\infty}\frac{(-1)^{n+1}}{2n-1}e^{i(2n-1)2\pi\xi}$$
$$\left.\times\left[e^{\lambda_{2n-1}(y-H)}+e^{-\lambda_{2n-1}y}\right]\right\}, \quad (37)$$

with negligible loss of accuracy for relatively large M and order-one ratio for H/L. For the boundary flux on the top and bottom walls, the same extrapolation technique, Eq. (24), is used. The interior derivatives $\partial\phi_{\text{ex}}/\partial x$ and $\partial\phi_{\text{ex}}/\partial y$ can be directly calculated from ϕ_{ex}. The distribution of ϕ_{LBE} at Pe = 20 with $H = L = 66$ and $\Delta_d = \Delta_w = \Delta = 0.5$ is very similar to that in Fig. 6 of [17] where a sinusoidal variation of wall temperature is imposed.

To examine the accuracy of the LBE solutions, the relative L_2-norm errors for the interior distribution of ϕ, the boundary flux $D\partial\phi/\partial y|_{y=H}$, and the interior derivatives $\partial\phi/\partial x$ and $\partial\phi/\partial y$ are computed. Figure 30 shows the errors at different τ_D values when $\Lambda = 1/8$ is fixed and $\Delta_d = \Delta_w = 0.5$. It is clear that the magnitude of the errors is governed by Λ once the resolution and Pe are fixed. This holds for both cases with continuous and discontinuous boundary conditions as shown in Figs. 30(a) and 30(b), respectively. As expected, the case with discontinuous boundary conditions has much higher error magnitude for all the L_2-norm errors computed. It is of particular interest to examine if the dependence of the solution on Λ holds when the boundary is placed in an arbitrary position in the lattice. Using the requirements given in Ref. [36] it is

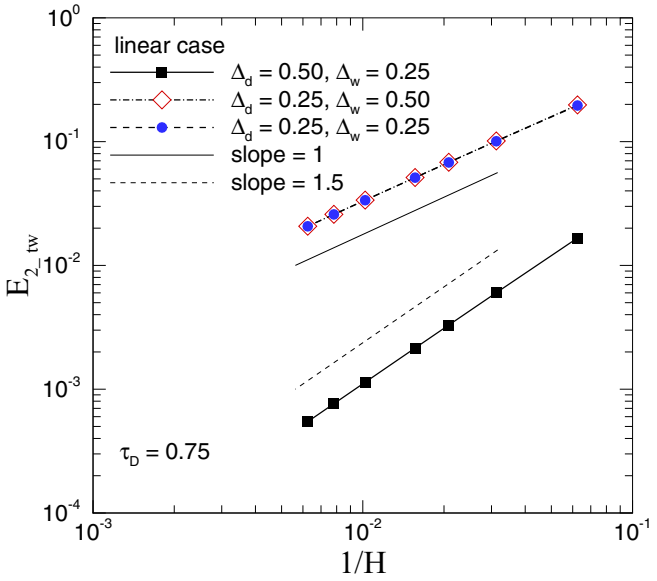

FIG. 27. Relative L_2-norm error E_{2_tw} of the boundary ϕ_w values versus $1/H$ for steady diffusion in the square block with the Neumann condition $f_{\text{linear}}(\eta)$ on the left wall and the discontinuity point off the lattice center.

found that scheme 3 in Eq. (10c) is able to satisfy the equivalent relations for the anti-bounce-back scheme and thus it would produce exactly the same nondimensional solution when Λ is fixed to $1/8$. Contrarily, schemes 1 and 2 in Eqs. (10a) and (10b) fail to satisfy these relations. Figure 31 shows the results for $\Delta_d = \Delta_w = 0.75$ for both continuous and discontinuous boundary conditions computed using these three schemes. Indeed the results from scheme 3 are independent of τ_D. Other

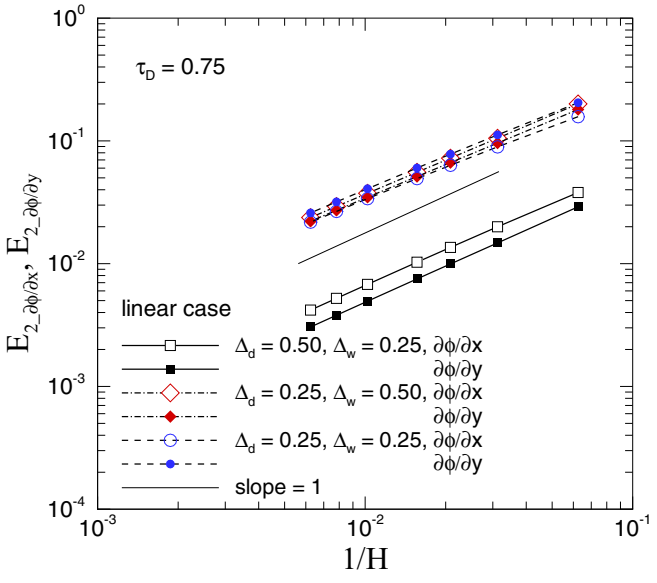

FIG. 28. Relative L_2-norm errors $E_{2\_\partial\phi/\partial x}$ and $E_{2\_\partial\phi/\partial y}$ of the interior derivatives versus $1/H$ for steady diffusion in the square block with the Neumann condition $f_{\text{linear}}(\eta)$ on the left wall and the discontinuity point off the lattice center.

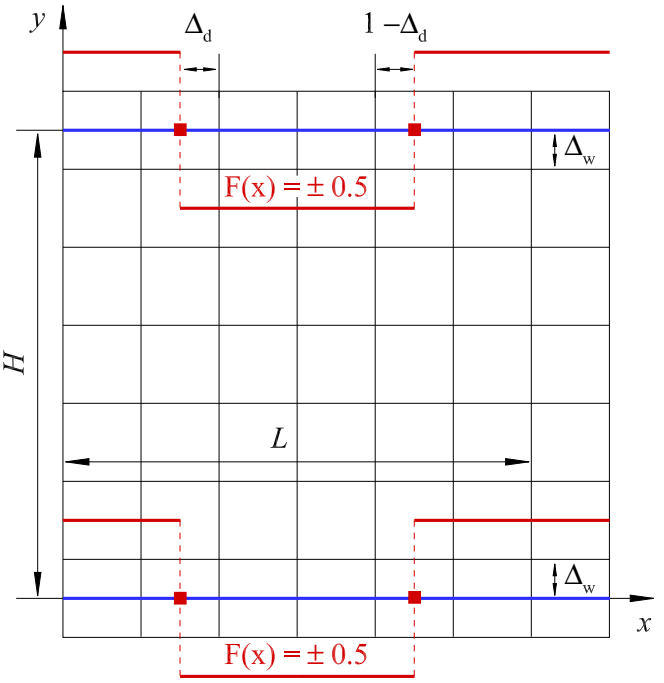

FIG. 29. Schematic depiction of the computational domain and lattice distribution for convection-diffusion in a channel with discontinuous boundary conditions.

values of Δ_d and Δ_w are also checked and the same solution behavior is observed.

Figures 32–34 show the L_2-norm errors versus the grid resolution for $\text{Pe} = 0$ (pure diffusion) and $\text{Pe} = 20$, 100 (moderate convection). First-order accurate solutions for the interior ϕ_{LBE} and zeroth-order accurate solutions for the interior derivatives are observed for all three cases with $\text{Pe} = 0$, 20, and 100. Similar to the diffusion problem presented in Sec. IV A 1 with the piecewise discontinuous function $f = f_{\text{linear}}(\eta)$ as a boundary condition, the boundary flux for $\text{Pe} = 0$ in this test also has exceptionally small relative errors. Only first-order accuracy is obtained for the boundary flux when a finite Pe(= 20, 100) is used, which is one degree lower than the quadratic convergence of the boundary flux computed for the diffusion problem in the block for $f = f_{\text{parab}}(\eta)$ and $f_{\text{sine}}(\eta)$ and $\Delta_d = \Delta_w = 0.5$. Finite convection results in a boundary layer near each of the horizontal walls, and a higher Pe implies a thinner boundary layer. Furthermore, the convection also results in asymmetry of the contours near the discontinuity points, making it more difficult to resolve the downstream region than the upstream region of the discontinuity due to the boundary layer effect. This is directly responsible for the change of the order of accuracy from second to first order for the normal boundary flux. The convection clearly brings in another important mechanism in affecting the transport and enhancement of the errors.

The combined effect of convection and discontinuity placement on the accuracy of the LBE results is elucidated in the contours for $\text{err} = \phi_{\text{LBE}} - \phi_{\text{ex}}$ in Figs. 35(a)–35(f) for $(\text{Pe}, \Delta_d) = (0, 0.5)$, $(0, 0.25)$, $(20, 0.5)$, $(20, 0.25)$, $(100, 0.5)$, and $(100, 0.25)$. For all six cases $\Delta_w = 0.5$ in the y direction is

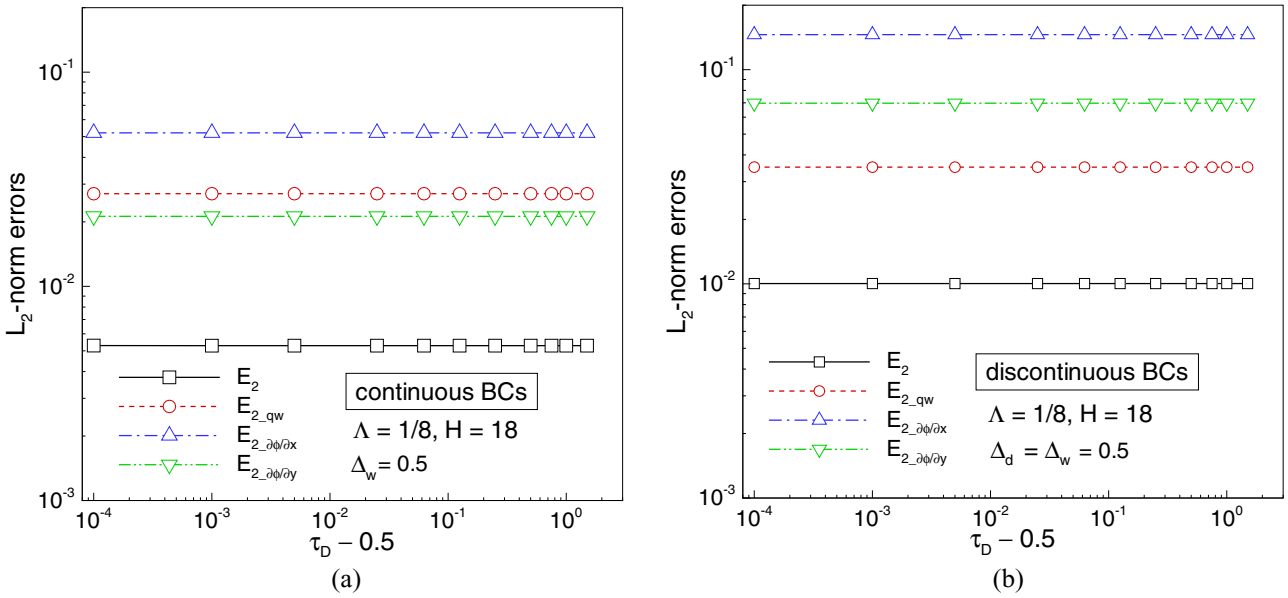

FIG. 30. Relative L_2-norm errors versus $(\tau_D - 0.5)$ for convection-diffusion in the channel at fixed $\Lambda = (\tau_D - 0.5)(\tau_p - 0.5) = 1/8$, Pe $= 20$, and $H = 18$ with (a) continuous boundary conditions $\phi_w(y = 0) = \phi_w(y = H) = \cos(2\pi x/L)$ and (b) discontinuous boundary conditions (see Fig. 29) on the horizontal walls.

used. For each Pe, there is a drastic increase in the magnitude of error when Δ_d changes from 0.5 to 0.25. On the other hand, for $\Delta_d = 0.5$, the error increases only by a factor of 2–3 when Pe changes from 0 to 100. This indicates that the error is much more sensitive to the placement of the discontinuity points within the lattice. For each nonzero Pe, the error contours of $\Delta_d = 0.5$ and 0.25 are very similar; the difference is in the magnitude caused by the discontinuity location. This is simply because the error in $\phi_{\rm LBE}$ is also governed by the same convection-diffusion equation for ϕ except that the source for generating the error at the discontinuity is much stronger with $\Delta_d = 0.25$ due to geometric asymmetry. Nevertheless, for all cases with $\Delta_d = 0.25$, first-order accuracy is obtained for the interior $\phi_{\rm LBE}$ at finite Pe. The accuracy for the boundary flux and interior derivatives remains to be zeroth order. Figures 36(a) and 36(b) also show how Δ_d and Δ_w affect the L_2-norm errors respectively for the interior $\phi_{\rm LBE}$, the boundary flux, and the interior derivatives at Pe $= 20$ and $H = 66$. In Figure 36(a) the case with $\Delta_d = 0.5$ has minimum errors for all four quantities and a sharp increase in the error magnitude is observed for E_2 and E_{2_qw} when the discontinuity location moves away from the midpoint $(\Delta_d = 0.5)$ to either side. In Fig. 36(b), E_2 and E_{2_qw} also have minimum values at $\Delta_w = 0.5$. The smallest error for $E_{2\_\partial\phi/\partial y}$ is noticed at $\Delta_w \sim 0.35$ and $E_{2\_\partial\phi/\partial x}$ decreases monotonically as Δ_w increases from 0.01 to 0.99; however, the differences between the $E_{2\_\partial\phi/\partial x}$ and $E_{2\_\partial\phi/\partial y}$ values at $\Delta_w = 0.5$ and their minimum values in the whole range of $0 \leqslant \Delta_w \leqslant 1$ are not significant. Overall, the placement of the discontinuity point at the lattice center with $\Delta_d = \Delta_w = 0.5$ is recommended.

It is also instructive to examine if using more distribution functions from neighboring lattice nodes would change the order of accuracy of the LBE solutions. To this end, the "third-order" Dirichlet boundary schemes by Ginzburg [37], which include five distributions at three lattice nodes near the boundary, are implemented (see Refs. [17,35] for implementation details). It should be noted that the correction term $F_q^{\rm p.c.}$ in [37] was not included in [17]. Here we correct this implementation and present the updated results in Figs. 37(a) and 37(b). For the continuous boundary conditions $\phi_w(y = 0) = \phi_w(y = H) = \cos(2\pi x/L)$, the results in Fig. 37(a) include the second-order boundary scheme in [17] (it reduces to anti-bounce-back at $\Delta = 0.5$), and the third-order schemes with or without the correction term. It is noted that second-order accuracy is obtained for all cases and by including the correction term the magnitude of the errors is significantly reduced. These third-order schemes with the correction term are also implemented for the present discontinuous boundary condition in Fig. 37(b), where first-order accuracy for E_2 is obtained for each case. Figure 38 also shows the variations of all the L_2-norm errors with Λ at Pe $= 20$ and $H = 34$ with the implementation of both the second-order and third-order boundary schemes. For most cases, the third-order scheme leads to slightly smaller error magnitude and the optimal Λ value is also at $\Lambda = 1/8$. Similar to the results in Fig. 12(a), the dependence of E_2 on Λ in Fig. 38 can also be well approximated by the power functions $E_2 \sim \{^{-0.086\sqrt{\Lambda}+0.035,\ \Lambda\leqslant 1/8,}_{0.154\sqrt{\Lambda}-0.064,\ \Lambda\geqslant 1/8}$ for the anti-bounce-back scheme and $E_2 \sim \{^{-0.067\sqrt{\Lambda}+0.029,\ \Lambda\leqslant 1/8,}_{0.118\sqrt{\Lambda}-0.049,\ \Lambda\geqslant 1/8}$ for the third-order scheme. Overall, the results in Figs. 37 and 38 indicate that the same order of accuracy is obtained for the second-order and third-order Dirichlet boundary schemes; and one can tune the adjustable parameter in the third-order schemes to reduce the error magnitude. The optimal choice of the adjustable parameters is out of the scope of this work and thus not pursued.

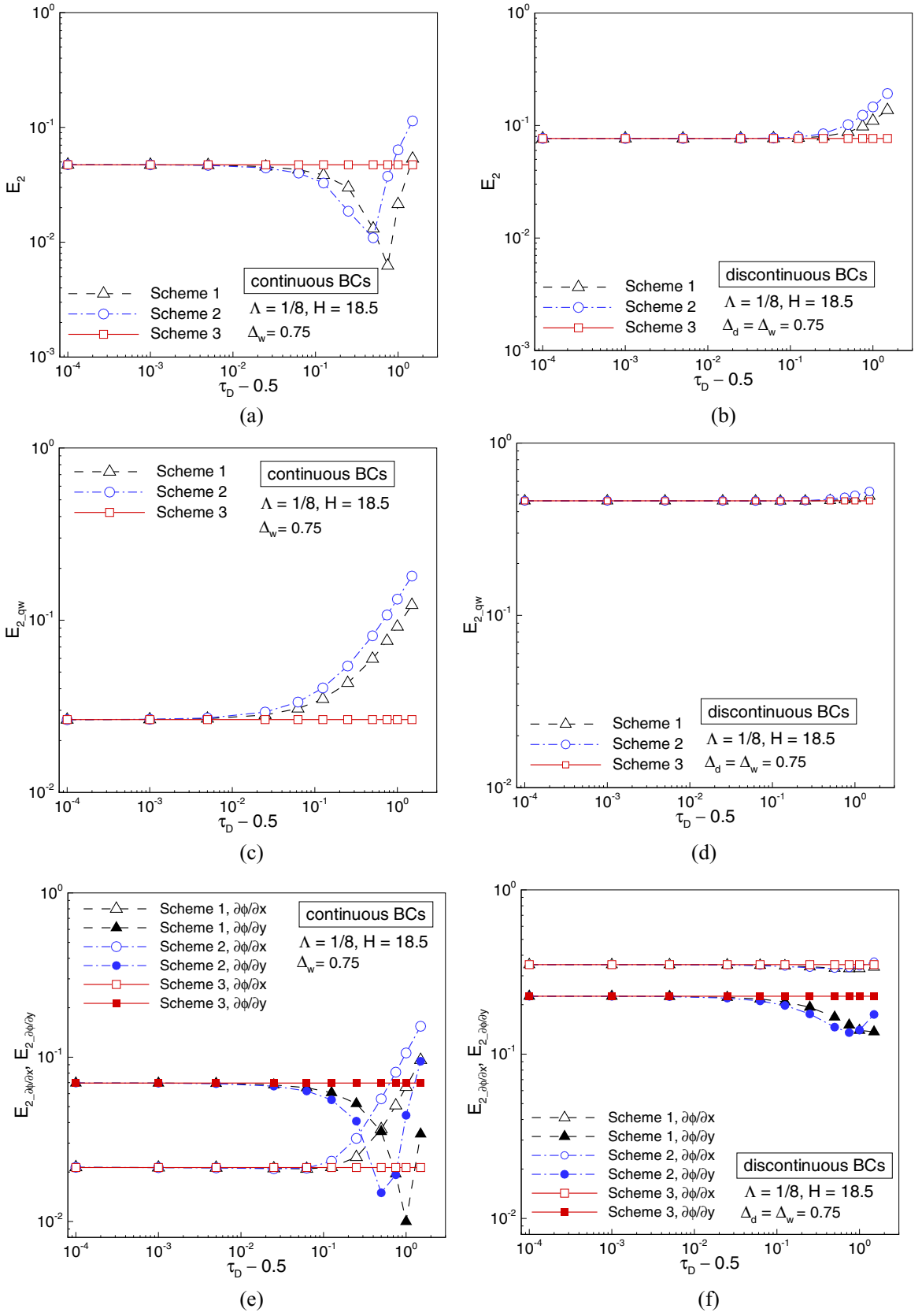

FIG. 31. Relative L_2-norm errors versus $(\tau_D - 0.5)$ for convection-diffusion in the channel at fixed $\Lambda = (\tau_D - 0.5)(\tau_p - 0.5) = 1/8$, Pe $=$ 20, $H = 18.5$, and $\Delta = 0.75$: (a) E_2, (c) E_{2_qw}, (e) $E_{2\_\partial\phi/\partial x}$ and $E_{2\_\partial\phi/\partial y}$ with continuous boundary conditions $\phi_w(y = 0) = \phi_w(y = H) = \cos(2\pi x/L)$, and (b) E_2, (d) E_{2_qw}, (f) $E_{2\_\partial\phi/\partial x}$ and $E_{2\_\partial\phi/\partial y}$ with discontinuous boundary conditions (see Fig. 29) on the horizontal walls.

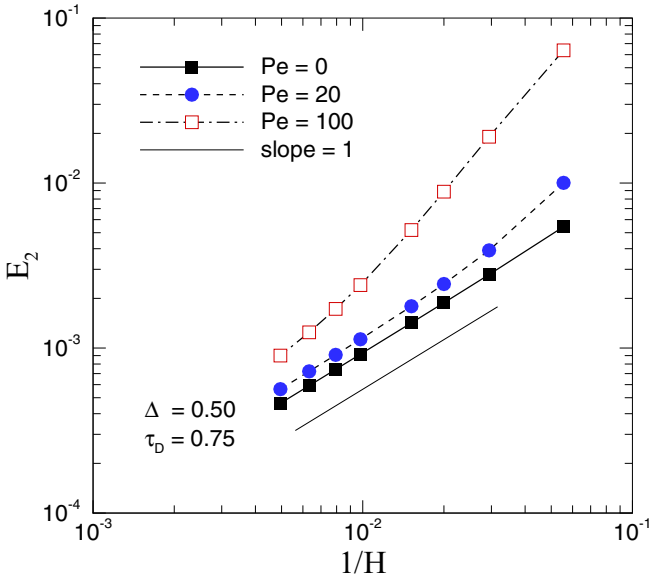

FIG. 32. Relative L_2-norm error E_2 of the interior distribution of ϕ versus the grid resolution $1/H$ for steady pure diffusion (Pe = 0) and convection-diffusion (Pe = 20, 100) in the channel with discontinuous Dirichlet boundary conditions.

2. *Discontinuous Neumann boundary condition*

For the Neumann problem, the boundary conditions in Eq. (34) are replaced by

$$\Phi_n|_{y=0} = -D\frac{\partial\phi}{\partial y}\bigg|_{y=0} = D\frac{F(x)}{H}, \tag{38a}$$

$$\Phi_n|_{y=H} = -D\frac{\partial\phi}{\partial y}\bigg|_{y=H} = -D\frac{F(x)}{H}, \tag{38b}$$

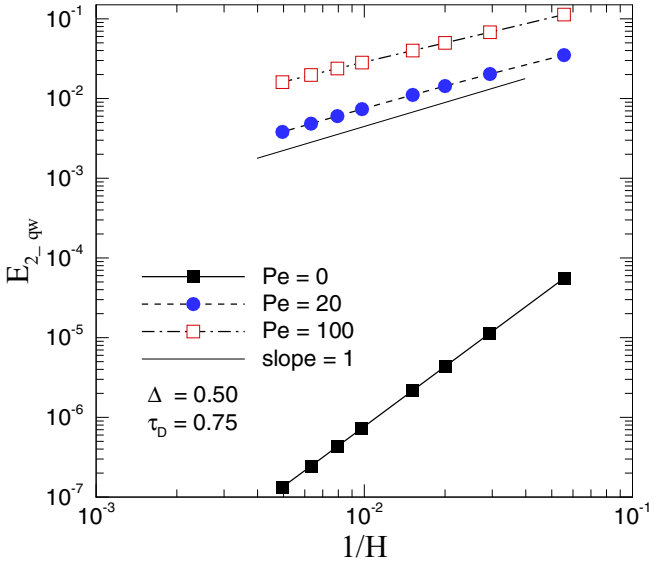

FIG. 33. Relative L_2-norm error E_{2_qw} of the boundary flux versus $1/H$ for steady pure diffusion (Pe = 0) and convection-diffusion (Pe = 20, 100) in the channel with discontinuous Dirichlet boundary conditions.

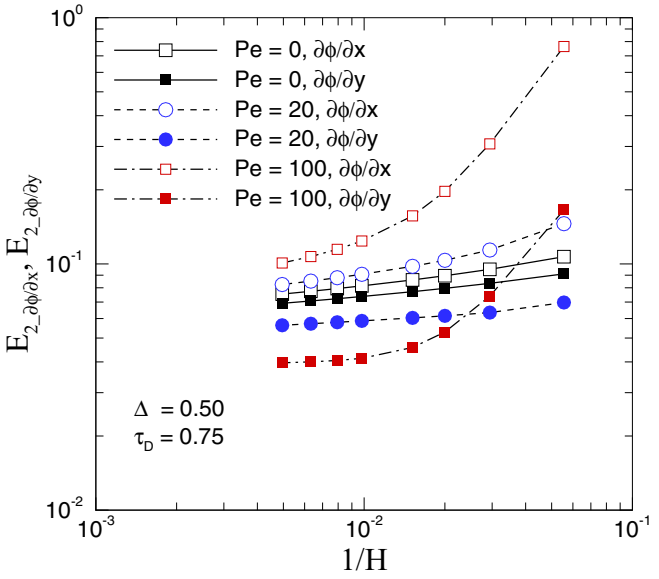

FIG. 34. Relative L_2-norm errors $E_{2\_\partial\phi/\partial x}$ and $E_{2\_\partial\phi/\partial y}$ of the interior derivatives versus $1/H$ for steady pure diffusion (Pe = 0) and convection-diffusion (Pe = 20, 100) in the channel with discontinuous Dirichlet boundary conditions.

where $F(x)$ is given in Eq. (34). The exact solution for ϕ can be expressed as

$$\begin{aligned}\phi_{\rm ex}(x,y) = \frac{2}{\pi H}{\rm Re}\Bigg\{&\sum_{n=1}^{M}\frac{(-1)^{n+1}}{(2n-1)\lambda_{2n-1}}e^{i(2n-1)2\pi\xi}\\ &\times\frac{e^{\lambda_{2n-1}y}+e^{\lambda_{2n-1}(H-y)}}{e^{\lambda_{2n-1}H}-1}\\ &+\sum_{n=M+1}^{N_\infty}\frac{(-1)^{n+1}}{(2n-1)\lambda_{2n-1}}e^{i(2n-1)2\pi\xi}\\ &\times[e^{\lambda_{2n-1}(y-H)}+e^{-\lambda_{2n-1}y}]\Bigg\}.\end{aligned} \tag{39}$$

The distribution of $\phi_{\rm LBE}$ for Pe = 20, $H = 66$, and $\Delta_d = \Delta_w = 0.5$ is very similar to that shown in Fig. 14 of [17]; thus they are not shown here. The relative L_2-norm errors for the interior distribution of ϕ, the boundary values (ϕ_w), and the interior derivatives ($\partial\phi/\partial x$ and $\partial\phi/\partial y$) are shown in Figs. 39–41 for $\Delta_d = \Delta_w = 0.5$. The results for both pure diffusion (Pe = 0) and moderate convection diffusion (Pe = 20, 100) are included. The orders-of-accuracy for these three quantities are consistent with those in the square block diffusion problem with discontinuous Neumann conditions and $\Delta_d = 0.5$, i.e., second-order accuracy for the interior field of ϕ, a superlinear order ~1.5 for the boundary values, and first-order accuracy for the interior derivatives in both directions are obtained for the present problem with all three Pe = 0, 20, and 100. Other combinations of Δ_d and Δ_w values are also examined and the same patterns for the orders-of-accuracy as in Figs. 26–28 for the diffusion problem are observed; thus they are not shown.

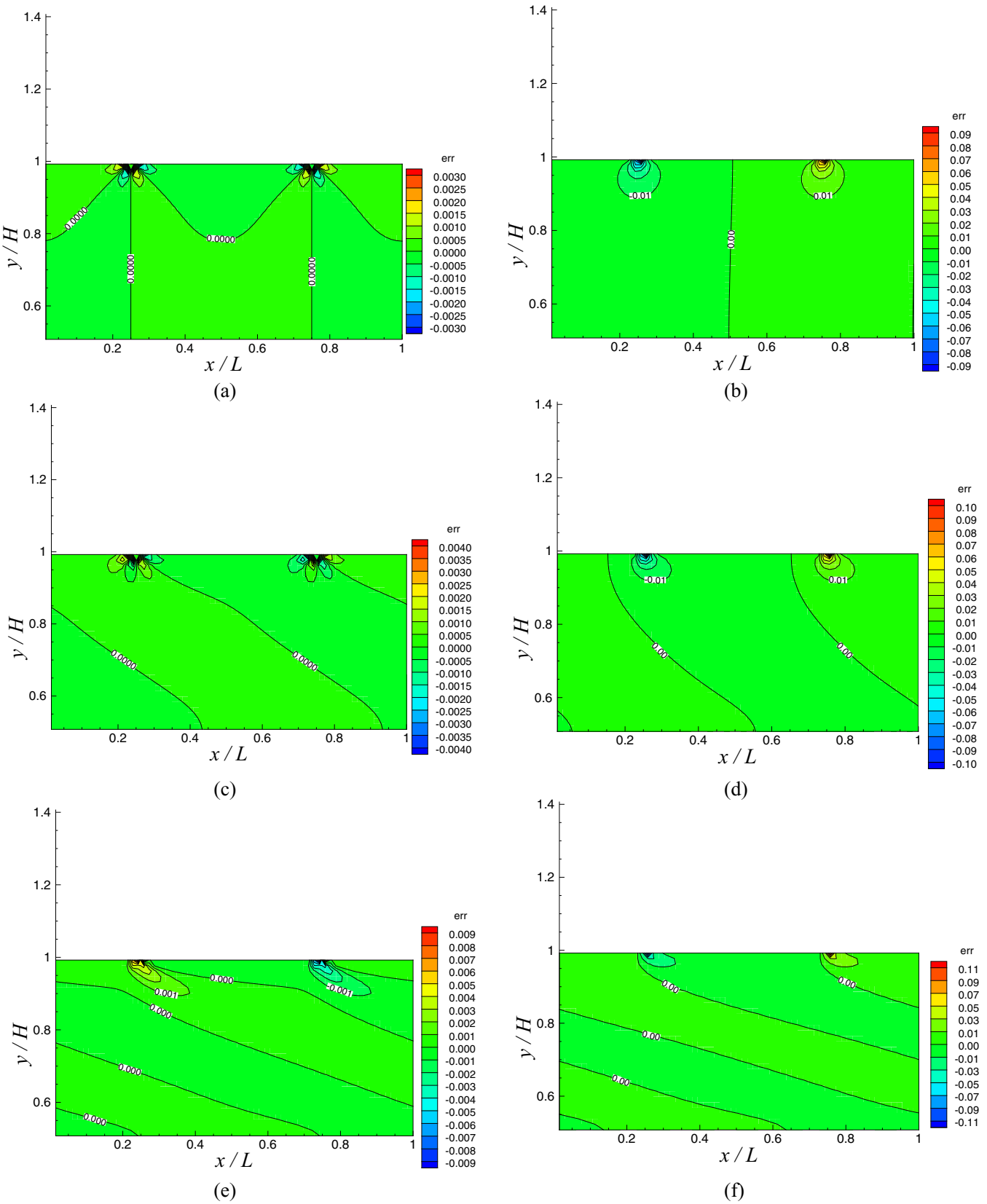

FIG. 35. Contours of the absolute errors of err $= \phi_{\mathrm{LBE}} - \phi_{\mathrm{ex}}$ in the upper half channel ($H = L = 66$) with discontinuous Dirichlet boundary conditions for (a) Pe $= 0$, $\Delta_d = 0.5$, (b) Pe $= 0$, $\Delta_d = 0.25$, (c) Pe $= 20$, $\Delta_d = 0.5$, (d) Pe $= 20$, $\Delta_d = 0.25$, (e) Pe $= 100$, $\Delta_d = 0.5$, and (f) Pe $= 100$, $\Delta_d = 0.25$.

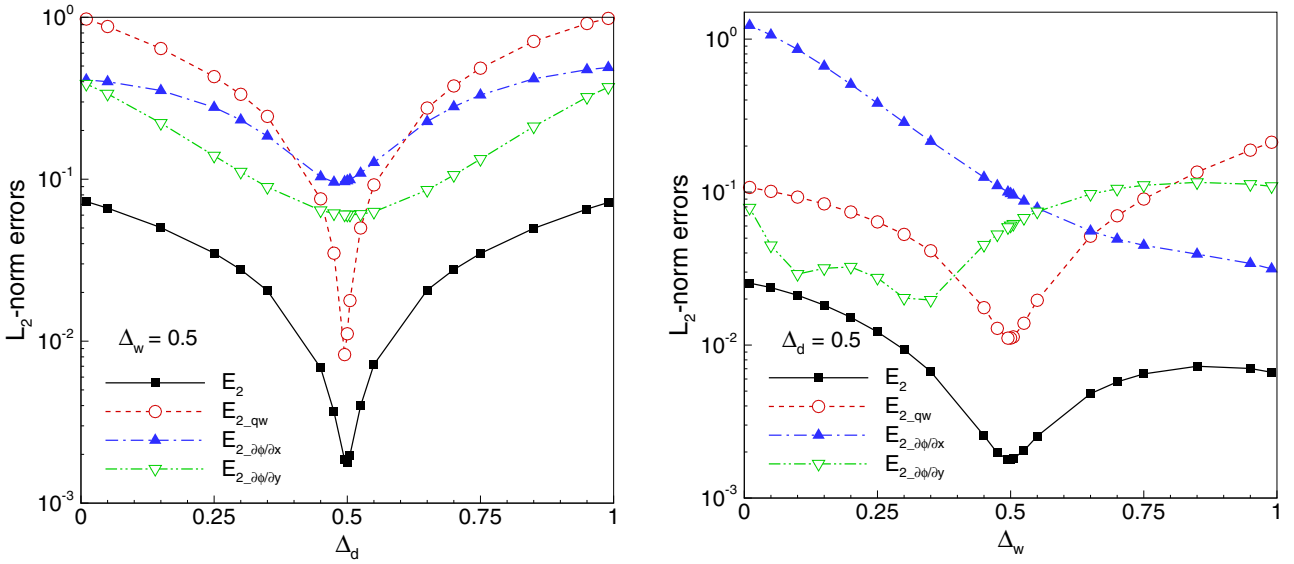

FIG. 36. Variations of the relative L_2-norm errors with (a) the lattice fraction Δ_d when $\Delta_w = 0.5$ and (b) the lattice fraction Δ_w when $\Delta_d = 0.5$, for the channel flow Dirichlet problem at Pe $= 20$.

C. Heat conduction in a circular cylinder

All the boundaries in the previous two tests involve straight walls. To investigate the combined effect of curved geometry and tangential-type boundary condition discontinuity on the order of accuracy of LBE solutions, steady heat conduction in a circular cylinder is considered next. The geometry and lattice distribution are depicted in Fig. 42. The imposed Dirichlet and Neumann boundary conditions have discontinuities at $\theta = 0$ and $\theta = \pi$. The specific lattice link fractions in both x and y directions for the lattice nodes next to the boundary are calculated (e.g., Δx and Δy for node P in Fig. 42) so that the boundary condition treatments in Eqs. (10) and (12) are implemented.

1. *Discontinuous Dirichlet boundary condition*

The discontinuous Dirichlet boundary condition is given by a unit step function

$$\phi_w(r = R,\theta) = \begin{cases} 1, & 0 < \theta < \pi, \\ 0, & \pi < \theta < 2\pi. \end{cases} \tag{40}$$

The exact solution for ϕ is

$$\phi_{\text{ex}}(r,\theta) = \frac{1}{2} + \frac{2}{\pi}\sum_{n=1}^{\infty} \frac{(r/R)^{2n-1}}{2n-1} \sin(2n-1)\theta, \tag{41}$$

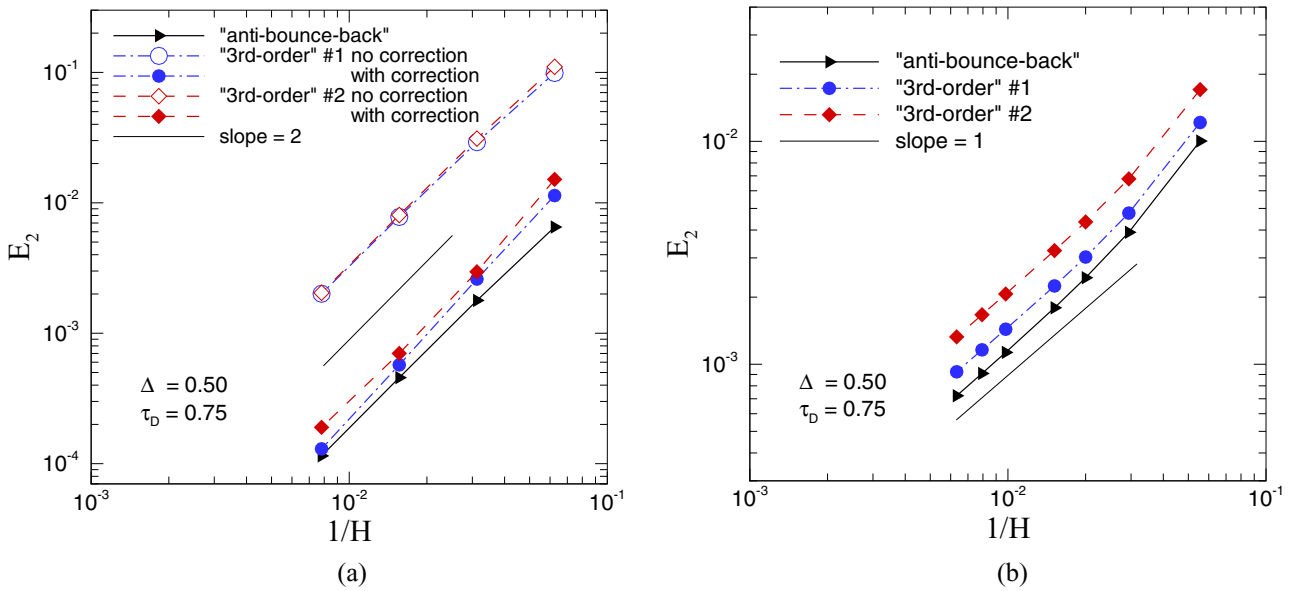

FIG. 37. Relative L_2-norm error E_2 versus the grid resolution $1/H$ for convection-diffusion (Pe $= 20$) in the channel with (a) continuous boundary conditions $\phi_w(y = 0) = \phi_w(y = H) = \cos(2\pi x/L)$ and (b) discontinuous boundary conditions (see Fig. 29) on the horizontal walls.

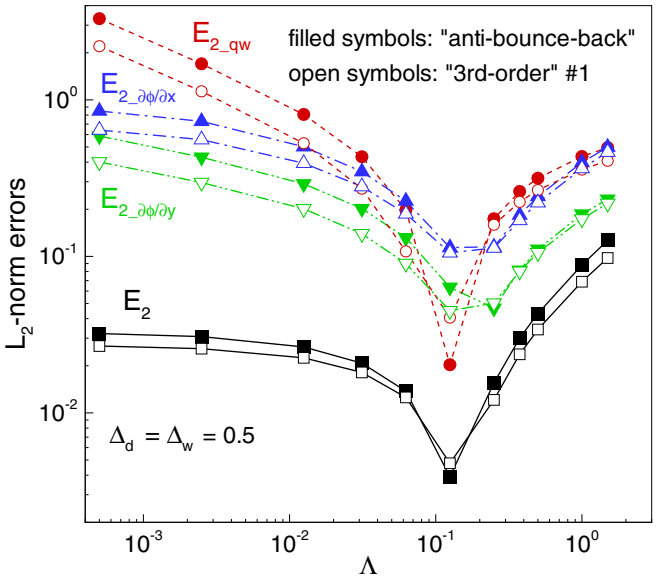

FIG. 38. Variations of the relative L_2-norm errors with $\Lambda = (\tau_D - 0.5)(\tau_p - 0.5)$ for convection-diffusion in the channel at Pe = 20.

and the radial and azimuthal derivatives are

$$\frac{\partial \phi_{\rm ex}}{\partial r}(r,\theta) = \frac{2}{\pi}\sum_{n=1}^{\infty}\frac{(r/R)^{2n-2}}{R}\sin(2n-1)\theta, \quad (42a)$$

$$\frac{1}{r}\frac{\partial \phi_{\rm ex}}{\partial \theta}(r,\theta) = \frac{2}{\pi}\sum_{n=1}^{\infty}\frac{(r/R)^{2n-1}}{r}\cos(2n-1)\theta. \quad (42b)$$

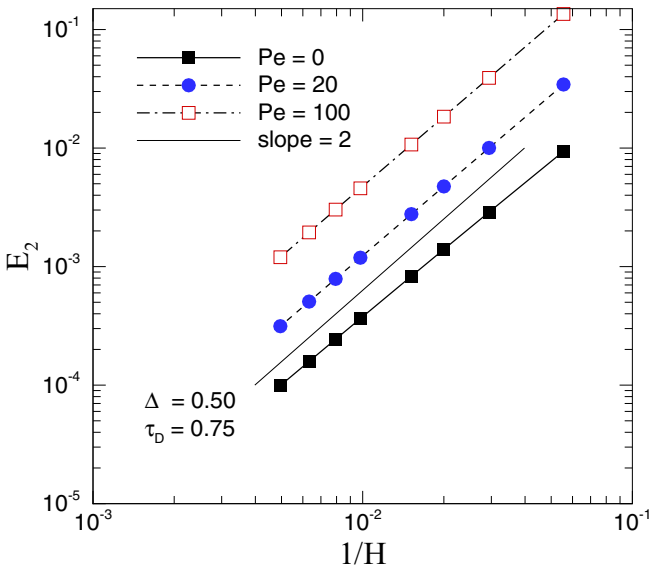

FIG. 39. Relative L_2-norm error E_2 of the interior distribution of ϕ versus $1/H$ for steady pure diffusion (Pe = 0) and convection-diffusion (Pe = 20, 100) in the channel with discontinuous Neumann boundary conditions.

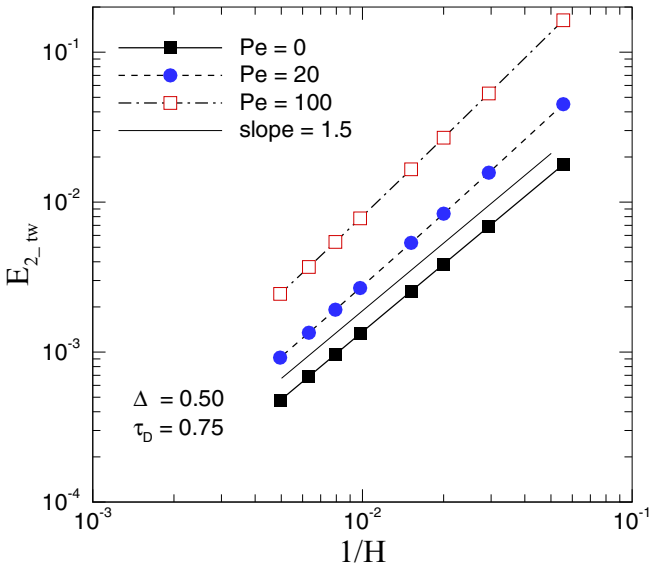

FIG. 40. Relative L_2-norm error $E_{2\_\rm tw}$ of the boundary ϕ_w values versus $1/H$ for steady pure diffusion (Pe = 0) and convection-diffusion (Pe = 20, 100) in the channel with discontinuous Neumann boundary conditions.

It is noted that the boundary fluxes cannot be obtained from Eq. (42) since the series do not converge at $r = R$, and the extrapolation in Eq. (24) is used again.

The three particular Dirichlet schemes in Eqs. (10a)–(10c) are directly implemented with the local link fractions calculated. Figures 43–45 show the L_2-norm errors for the interior distribution of ϕ, the boundary flux, and the interior derivatives, as defined in Eqs. (27)–(29), respectively, versus the grid resolution $1/R$ when $\Delta_d = \Delta_w = 0.5$ is used. The boundary nodes in Eq. (29) for this test include all the

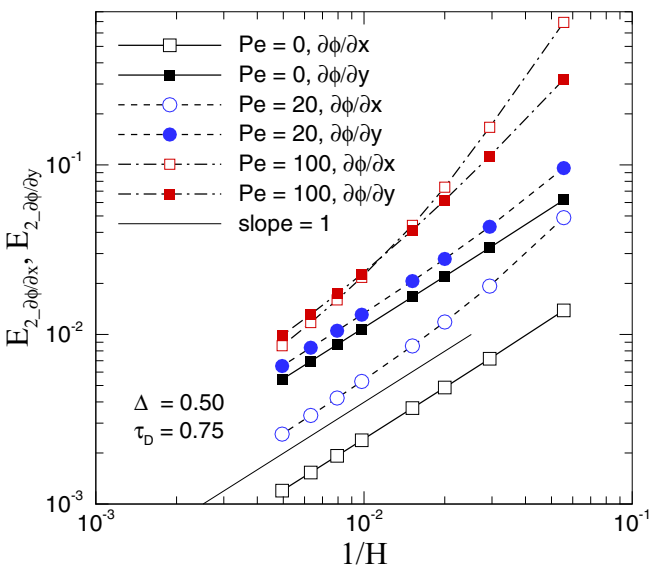

FIG. 41. Relative L_2-norm errors $E_{2\_\partial\phi/\partial x}$ and $E_{2\_\partial\phi/\partial y}$ of the interior derivatives versus $1/H$ for steady pure diffusion (Pe = 0) and convection-diffusion (Pe = 20, 100) in the channel with discontinuous Neumann boundary conditions.

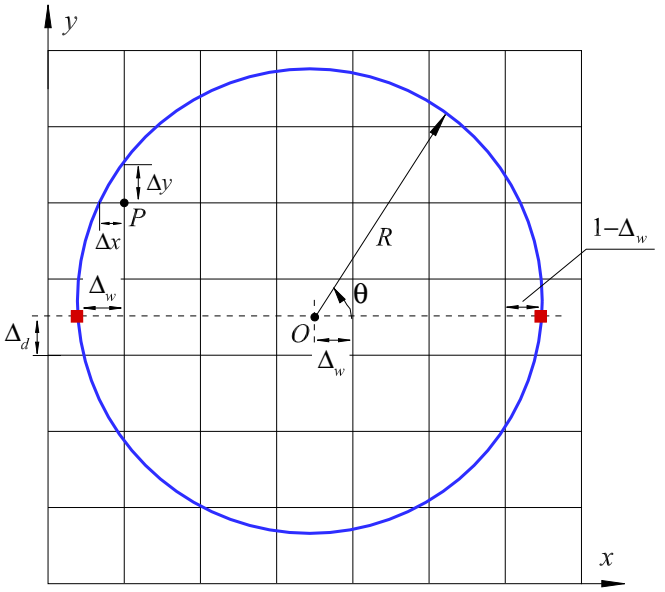

FIG. 42. Schematic depiction of the lattice distribution for diffusion in a circular plane. The circular geometry is preserved by calculating the exact link fraction Δ values in both x and y directions for the interior nodes next to the boundary, e.g., Δx and Δy for P.

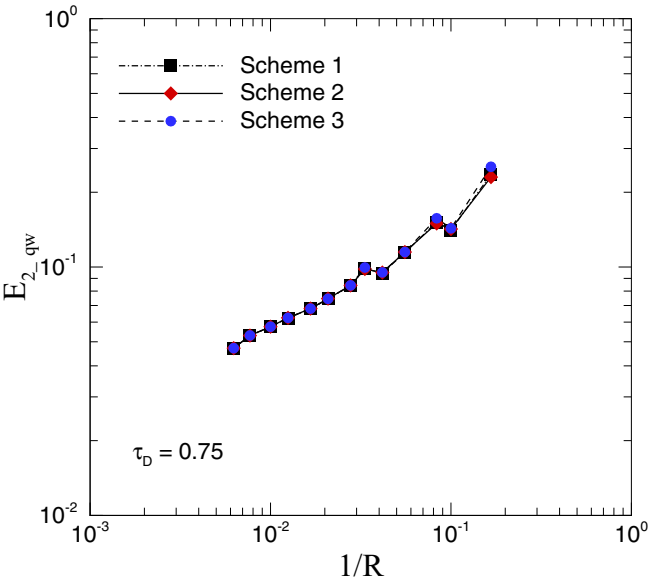

FIG. 44. Relative L_2-norm error E_{2_qw} of the boundary flux versus $1/R$ for steady diffusion in the circular plane with a discontinuous Dirichlet boundary condition.

intersection nodes by the lattice velocity vectors in both x and y directions. It is also emphasized that the boundary flux from the LBE computation is evaluated in the Cartesian x and y directions parallel to the intersecting lattice velocity vectors [see Eq. (13)] so that the extrapolated analytical boundary fluxes in the normal and tangential directions are projected to the x and y directions. The results in Figs. 43–45 from using the three Dirichlet schemes are very close to each other at $R > 10$. First-order accuracy for the interior ϕ values and zeroth-order accuracy for the interior derivatives are clearly seen in Figs. 43 and 45. The numerical convergence of the boundary flux in Fig. 44 is also close to zeroth-order asymptotically. The respective orders-of-accuracy are the same as those for the square block diffusion problem when the discontinuity point is placed away from the lattice center.

Ginzburg and d'Humieres [31,39] pointed out that when a boundary scheme is incompatible with that for the interior solution, an accommodation layer will develop and the "accommodation" in the LBE method manifests itself differently for different orders of the incompatibility with the bulk nonequilibrium, from relatively smooth nonequilibrium

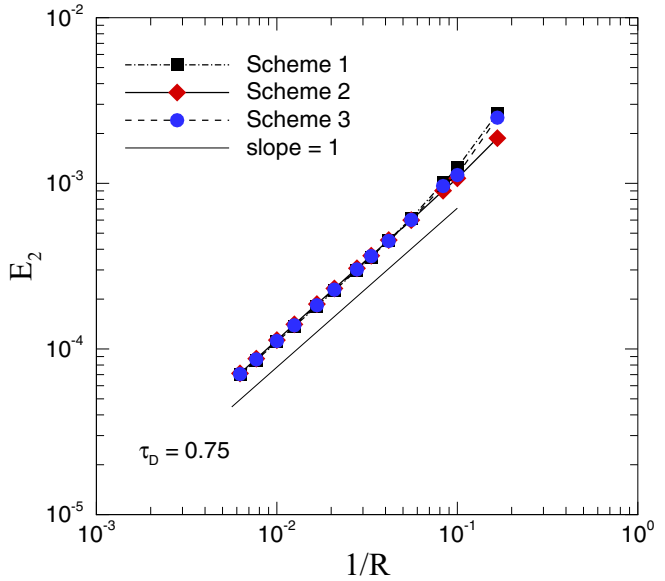

FIG. 43. Relative L_2-norm error E_2 of the interior ϕ values versus the grid resolution $1/R$ for steady diffusion in the circular plane with a discontinuous Dirichlet boundary condition.

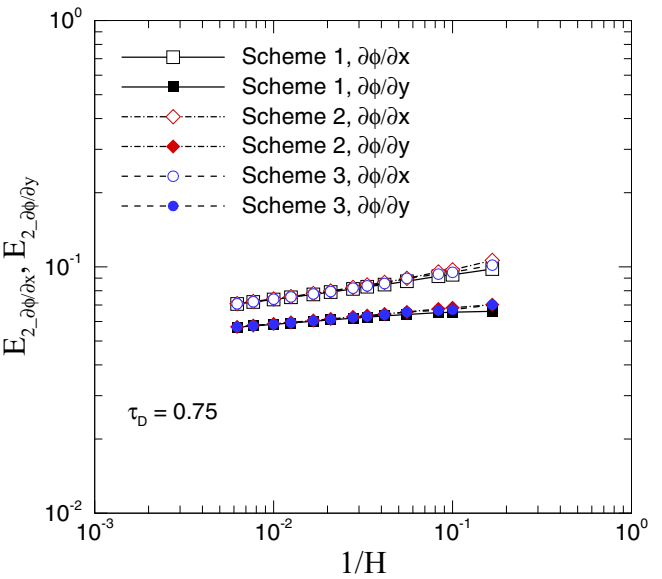

FIG. 45. Relative L_2-norm errors $E_{2\_\partial\phi/\partial x}$ and $E_{2\_\partial\phi/\partial y}$ of the interior derivatives versus $1/R$ for steady diffusion in the circular plane with a discontinuous Dirichlet boundary condition.

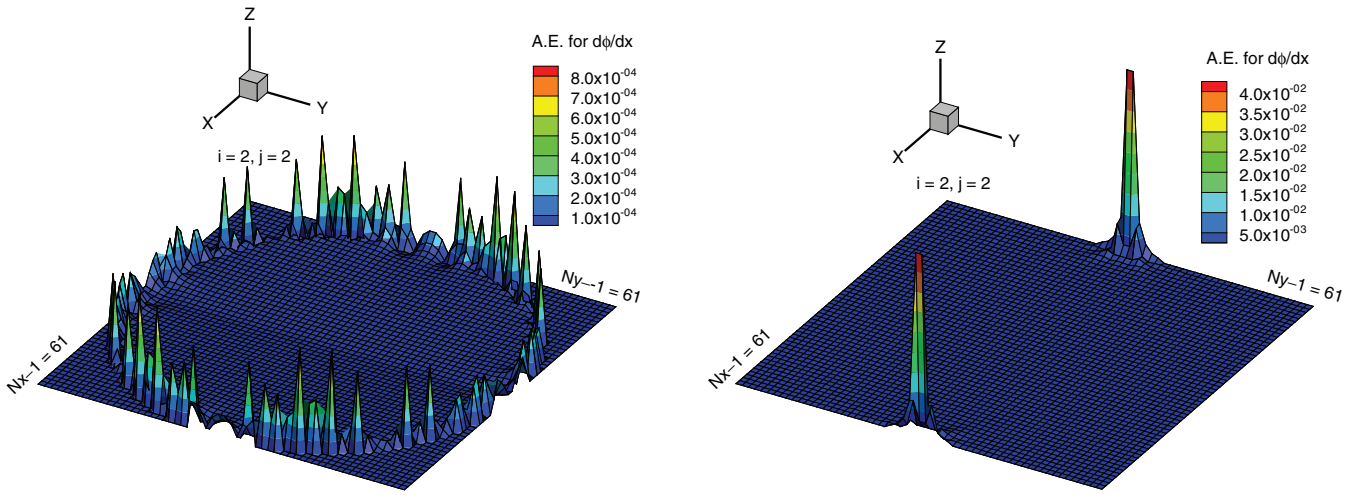

FIG. 46. Distribution of the absolute error for the interior derivative A.E. $= |(\partial\phi/\partial x)_{\rm LBE} - (\partial\phi/\partial x)_{\rm ex}|$ for diffusion in a circular domain ($R = 30$) with (a) continuous boundary condition $\phi_w(r = R,\theta) = \cos(4\theta)$ and (b) discontinuous boundary condition in Eq. (40).

layers which do not impact the macroscopic solution, e.g., [40], to jumps in boundary and interface derivatives for inaccurate collision strategies with discontinuous coefficients [31,32]. We also observed that in the cases with continuous boundary conditions [17] or normal discontinuities (jumps) across the interface [33], the presence of incompatibility and accommodation layer does not lead to degradation of accuracy when straight wall is involved for Dirichlet problems. For curved boundary problems, the order of accuracy for the field of ϕ is unaffected by the presence of the accommodation layer, while that for the interior derivative decreases from 2 to 1.5 (superlinear) when a continuous Dirichlet condition is imposed on the surface of a circular cylinder [17]. Figure 46(a) shows the distribution of the absolute error for the interior derivative in the x direction, i.e., A.E. $= |(\partial\phi/\partial x)_{\rm LBE} - (\partial\phi/\partial x)_{\rm ex}|$, at $R = 30$ and $\Delta_d = \Delta_w = 0.5$ (see Fig. 42) for the Dirichlet condition of $\phi_w(r = R,\theta) = \cos(4\theta)$. The presence of such an accommodation layer is clearly demonstrated in this example. When the resolution R increases, the magnitude of the error in the accommodation layer decreases as $R^{-1.5}$. In contrast, for the Dirichlet problem with tangential-type discontinuous boundary condition given by Eq. (40), the error for $\partial\phi/\partial x$ shown in Fig. 46(b) has two simple peaks near the discontinuities. The two peaks have much larger magnitude than those in Fig. 46(a), although both problems have order one variation in the bourndary values. Varying the resolution R does not change the magnitude of the two peaks as the derivatives near the discontinuities remain invariant with R. Thus the error caused by the discontinuity clearly dominates that caused by the boundary scheme incompatibility. It is concluded that for Dirichlet problems with tangential-type boundary condition discontinuity on curved geometry, the increase in the magnitude of numerical error and/or degradation in the order-of-accuracy are mainly due to the presence of the discontinuity.

The placement of the discontinuity point in the lattice for curved geometry is also studied by shifting the whole circle in the lattice structure (see Fig. 42). For a representative radius $R = 36$, the L_2-norm errors for the interior $\phi_{\rm LBE}$ and boundary flux are $(E_2, E_{2\_\rm qw}) = (3.07 \times 10^{-4}, 8.43 \times 10^{-2})$, $(1.81 \times 10^{-3}, 1.33 \times 10^{-1})$, $(7.47 \times 10^{-3}, 4.80 \times 10^{-1})$, and $(7.27 \times 10^{-3}, 4.90 \times 10^{-1})$ for $(\Delta_d, \Delta_w) = (0.5, 0.5)$, $(0.5, 0.25)$, $(0.25, 0.5)$, and $(0.25, 0.25)$, respectively. The same increasing trend is observed for the L_2-norm errors for the interior derivatives. Clearly when the discontinuity point is moved away from the lattice center, a remarkable increase in the error magnitude is noticed. And the influence of the intersection fraction Δ_d is more significant than that of Δ_w, which is consistent with the results in the previous two tests.

2. *Discontinuous Neumann boundary condition*

For the Neumann problem, the boundary condition in Eq. (40) is changed to

$$\Phi_n = -D\frac{\partial\phi}{\partial r}\bigg|_{r=R} = \begin{cases} -D/R, & 0 < \theta < \pi, \\ D/R, & \pi < \theta < 2\pi. \end{cases} \tag{43}$$

The exact solution becomes

$$\phi_{\rm ex}(r,\theta) = \frac{4}{\pi}\sum_{n=1}^{\infty}\frac{(r/R)^{2n-1}}{(2n-1)^2}\sin(2n-1)\theta. \tag{44}$$

The discontinuous Neumann boundary condition in Eq. (43) also involves nonzero tangential flux along the azimuthal direction on the curved boundary. The Cartesian decomposition method [17,18], which first converts the normal boundary flux Φ_n into the flux $\Phi_{n\tilde{\alpha}}$ in the discrete lattice velocity direction, and then uses the Neumann scheme in Eq. (12), are thus implemented. Three particular schemes were examined in [17] with their corresponding choices of the adjustable coefficient c_{d_1} as in Eqs. (10a)–(10c). Using those three particular schemes, Figs. 47–49 show the L_2-norm errors for the interior distribution of ϕ, the boundary ϕ_w values, and the interior derivatives, respectively, when $\Delta_d = \Delta_w = 0.5$ is used. First-order accuracy is observed for all cases and the three boundary schemes give very close numerical results for each quantity investigated.

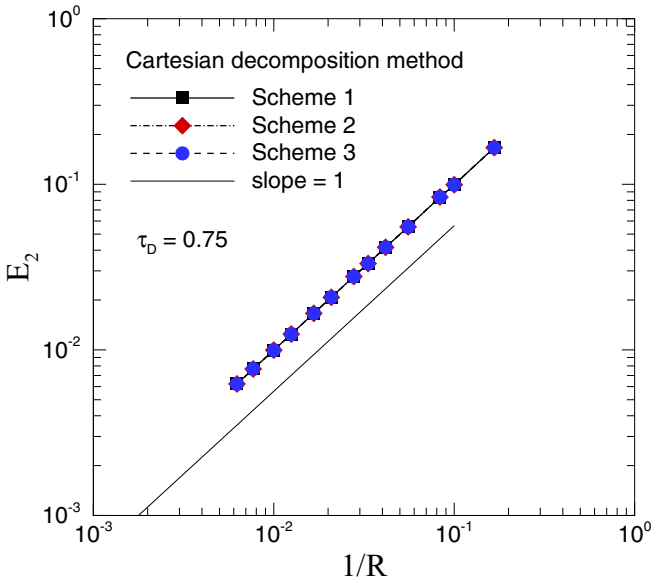

FIG. 47. Relative L_2-norm error E_2 of the interior ϕ values versus $1/R$ for steady diffusion in the circular plane with a discontinuous Neumann boundary condition.

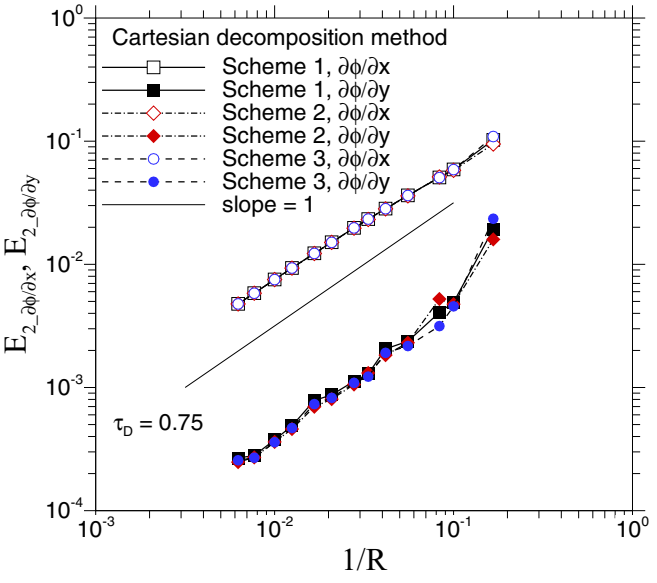

FIG. 49. Relative L_2-norm errors $E_{2\_\partial\phi/\partial x}$ and $E_{2\_\partial\phi/\partial y}$ of the interior derivatives versus $1/R$ for steady diffusion in the circular plane with a discontinuous Neumann boundary condition.

It should be noted that for Neumann problems with curved geometry and nonzero tangential flux, even with continuous normal flux distribution, the Cartesian decomposition method would result in first-order accuracy for the interior and boundary ϕ values [17,19,20]. To separate the contributions of the wall flux discontinuity and the Cartesian decomposition method on the order of accuracy of the LBE results, another test for the same problem is conducted by applying the exact boundary fluxes $\Phi_{n\bar{\alpha}}$ in the x and y directions following the similar test in [17], where it was verified that second-order accuracy could be obtained for the interior and boundary ϕ values as well as for the interior derivatives if the exact $\Phi_{n\bar{\alpha}}$ values were used. In the present test, the tangential flux on the circular boundary is calculated from Eq. (44) at $r = R$. Both the normal flux given by Eq. (43) and computed tangential fluxes determine the precise $\Phi_{n\bar{\alpha}}$. All results for E_2, E_{2_tw}, $E_{2\_\partial\phi/\partial x}$, and $E_{2\_\partial\phi/\partial y}$ obtained from this test are very close to those in Figs. 47–49 for each R value and thus not shown. It is thus concluded that the first-order accuracy in Figs. 47–49 is attributed to the tangential-type boundary condition discontinuity on the curved geometry; the Cartesian decomposition method has a much smaller impact on the error than that caused by the normal wall flux discontinuity.

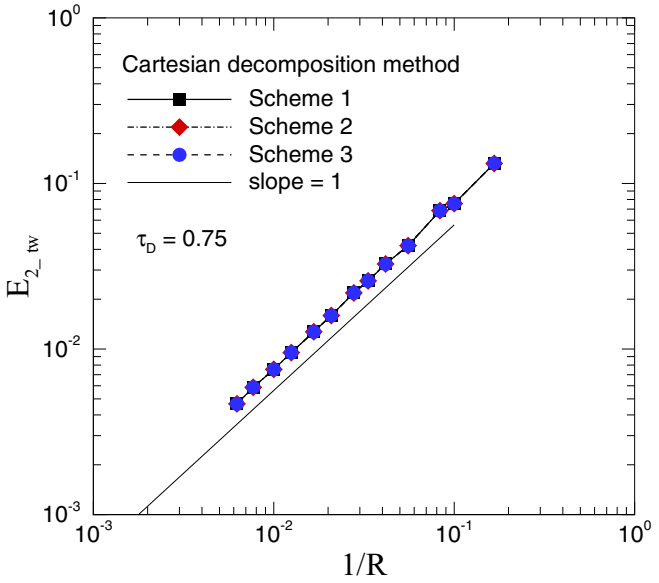

FIG. 48. Relative L_2-norm error E_{2_tw} of the boundary ϕ_w values versus $1/R$ for steady diffusion in the circular plane with a discontinuous Neumann boundary condition.

For both Dirichlet and Neumann problems with curved geometry, the errors in the LBE solutions caused by the tangential-type boundary condition discontinuities are much higher than those by the particular boundary schemes, as also demonstrated by the very close error magnitude in Figs. 43–45 and 47–49 for schemes 1, 2, and 3.

To summarize, the orders-of-accuracy for the various quantities of interest from those three tests are listed in Table I.

V. DIFFERENCE BETWEEN NORMAL DISCONTINUITY ACROSS AN INTERFACE AND TANGENTIAL DISCONTINUITY ALONG A BOUNDARY

The present study focuses on the "tangential discontinuity" *along* the boundary, as opposed to the "normal discontinuity" *across* the interface. It is important to recognize that these two types of boundary condition discontinuities are fundamentally different. In [31–33] the effects of normal discontinuities in ϕ and $\partial\phi/\partial n$ across the interface have been investigated. One can theoretically (based on the analysis of the distribution functions within the LB framework) derive the relationships between the "known" and "unknown" distributions near the interface by taking into account the physical constraints, e.g., the governing equations on each phase adjacent the interface,

TABLE I. Numerical accuracy in LBE computation for convection-diffusion with discontinuous Dirichlet or Neumann boundary conditions (ϕ denotes temperature or concentration, Δ_d and Δ_w denote the lattice link fractions at the discontinuity point $\mathbf{x}_d$ along the tangential and normal directions of the boundary, respectively).

	Interior distribution of ϕ	Boundary flux	Boundary ϕ value	Interior derivatives
1. Discontinuous Dirichlet condition				
a. Boundary aligned with lattice vector with $\mathbf{x}_d$ at lattice center ($\Delta_d = \Delta_w = 0.5$)	1st order	2nd order[a] 1st order[b]		0th order
b. Boundary aligned with lattice vector with $\mathbf{x}_d$ off lattice center ($\Delta_d \neq 0.5$ or $\Delta_w \neq 0.5$)	1st order	0th order		0th order
c. Curved boundary	1st order	0th order		0th order
2. Discontinuous Neumann condition				
a. Boundary aligned with lattice vector with $\Delta_d = 0.5, 0 \leqslant \Delta_w \leqslant 1$	2nd order		Superlinear Order ~1.5	1st order
b. Boundary aligned with lattice vector with $\Delta_d \neq 0.5, 0 \leqslant \Delta_w \leqslant 1$	1st order		1st order	1st order
c. Curved boundary	1st order		1st order	1st order

[a]Pure diffusion problems.
[b]General convection diffusion problems.

and the particular discontinuity condition at the interface. For instance, Ref. [32] presented the detailed analyses for two types of interface tracking, "explicit interface" and "implicit interface," for both hydrodynamic and advection-diffusion problems with discontinuous interface conditions. In the recent work [33], we have developed an interface treatment for both temperature and/or flux discontinuities (jumps) across the interface in the LB method. The second-order accuracy for straight interfaces was verified and the effect of curved geometry on the accuracy of the LBE solution was also presented in [33].

However, for the tangential discontinuity along the boundary considered in this work, such simple relations across the discontinuity do not exist. The local problem becomes two dimensional with the errors originating from the discontinuity on the boundary and propagating in all directions as shown in Figs. 4, 21, 35, and 46. On the contrary, the local problem for the normal discontinuity across the interface considered in [31–33] is essentially one dimensional from one subdomain to the other; there is no large variation along the interface. In fact, if the flux discontinuity appears only on part of the interface of two materials the tangential type of boundary condition discontinuity in the present study will be observed. A much larger error would be encountered.

It is also worth noticing that for tangential discontinuity problems, the degradation of the numerical accuracy due to the discontinuity is much more severe than encountered in the normal discontinuity type. As in the first test with a discontinuous Dirichlet condition on the straight boundary located halfway ($\Delta = 0.5$) in the lattice, the interior solution and its derivative have only first-order and zeroth-order accuracy, respectively; they are considerably worse than the second-order LBE solutions in [33] with both temperature and flux jumps across the interface.

VI. CONCLUSIONS

The effects of tangential-type discontinuities in Dirichlet and Neumann boundary conditions on the accuracy of numerical solutions using the lattice Boltzmann equation (LBE) method for thermal and mass transport are investigated. For straight boundaries that are aligned with the lattice velocity vectors, the discontinuous Dirichlet condition reduces the accuracy of the interior temperature (concentration) field from second to first order; while its second-order accuracy is preserved for discontinuous Neumann conditions when the discontinuity point is placed halfway in the lattice along the tangential direction of the boundary. The effect of discontinuity on the accuracy of LBE solutions in Dirichlet problems is stronger than that in Neumann problems. This is also demonstrated by the zeroth- and first-order accuracy of interior derivatives for the problems with discontinuous Dirichlet and Neumann boundary conditions, respectively.

For Dirichlet problems with a finite jump on the boundary values, the local solution for the derivatives can be described by a singular dipole model. The LBE solution for the derivatives on the lattice scale largely remains invariant with changing resolution, which is consistent with the dipole model. The local errors for the LBE derivatives are also invariant with respect to the resolution. The present results for the local derivative errors should be generally applicable for Laplace equations with finite boundary value jumps in Dirichlet problems. The

transfer of the errors in the individual microscopic distribution functions to those in the macroscopic value and its derivatives is scrutinized to reveal the cause for the deteriorated accuracy.

The placement of discontinuity points away from the lattice center results in either a degradation in the order of accuracy or a significant increase in the magnitude of the error. Thus it is highly preferable to place the discontinuity point at the lattice center and keep the straight walls aligned with the lattice directions.

The convection has a strong effect on the accuracy of LBE solutions in the presence of boundary condition discontinuities. This can be clearly observed compared to the pure diffusion problem with the discontinuity placed at the center of the lattice. The convection reduces the accuracy for boundary flux from second to first order in the Dirichlet problem due to the asymmetry of the solution field with respect to the discontinuity position caused by convection. The error magnitude in general increases with increasing Péclet number. When the discontinuity point is moved away from the lattice center, however, the increase in the absolute error caused by this off-center placement of the discontinuity is far greater than that caused by the change in the Péclet number from 0 to 100. It is strongly suggested that in arranging the lattice structure one should make every effort possible to place the discontinuity at the center of the lattice.

For curved geometry, the tangential-type discontinuous Dirichlet condition results in a first-order accurate temperature (concentration) field and zeroth-order accurate boundary flux and interior derivatives. The degradation in the accuracy for the interior derivative caused by the boundary discontinuity is much more significant than that caused by the incompatibility between the boundary condition treatment and the solution scheme for the interior domain. For Neumann problems, the discontinuity in the boundary condition causes the interior and boundary temperatures (concentrations) and their interior derivatives to be first-order accurate. The placement of a discontinuity point in the lattice structure is also critical for curved boundaries and it is recommended that the tangential-type boundary condition discontinuity be placed at the lattice center.

ACKNOWLEDGMENT

This paper was prepared with the support of the U.S. Department of Energy, ARPA-E, under Award No. DE-AR0000184.

[1] F. J. Alexander, S. Chen, and J. D. Sterling, Lattice Boltzmann thermohydrodynamics, Phys. Rev. E **47**, R2249 (1993).

[2] E. G. Flekky, Lattice Bhatnagar-Gross-Krook models for miscible fluids, Phys. Rev. E **47**, 4247 (1993).

[3] Y. Chen, H. Ohashi, and M. Akiyama, Thermal lattice Bhatnagar-Gross-Krook model without nonlinear deviations in macrodynamic equations, Phys. Rev. E **50**, 2776 (1994).

[4] X. Shan, Simulation of Rayleigh-Benard convection using a lattice Boltzmann method, Phys. Rev. E **55**, 2780 (1997).

[5] X. He, S. Chen, and G. D. Doolen, A novel thermal model for the lattice Boltzmann method in incompressible limit, J. Comput. Phys. **146**, 282 (1998).

[6] P. Lallemand and L.-S. Luo, Theory of the lattice Boltzmann method: Acoustic and thermal properties in two and three dimensions, Phys. Rev. E **68**, 036706 (2003).

[7] R. G. M. van der Sman and M. H. Ernst, Convection-diffusion lattice Boltzmann scheme for irregular lattices, J. Comput. Phys. **160**, 766 (2000).

[8] Z. Guo, C. Zheng, and B. Shi, Thermal lattice Boltzmann equation for low Mach number flows: Decoupling model, Phys. Rev. E **75**, 036704 (2007).

[9] B. Servan-Camas and F. T.-C. Tsai, Lattice Boltzmann method with two relaxation times for advection-diffusion equation: Third order analysis and stability analysis, Adv. Water Resour. **31**, 1113 (2008).

[10] B. C. Shi and Z. Guo, Lattice Boltzmann model for nonlinear convection-diffusion equations, Phys. Rev. E **79**, 016701 (2009).

[11] A. Mezrhab, M. A. Moussaoui, M. Jami, H. Naji, and M. Bouzidi, Double MRT thermal lattice Boltzmann method for simulating convective flows, Phys. Lett. A **374**, 3499 (2010).

[12] H. Yoshida and M. Nagaoka, Multiple-relaxation-time lattice Boltzmann model for the convection and anisotropic diffusion equation, J. Comput. Phys. **229**, 7774 (2010).

[13] I. Ginzburg, D. d'Humières, and A. Kuzmin, Optimal stability of advection-diffusion lattice Boltzmann models with two relaxation times for positive/negative equilibrium, J. Stat. Phys. **139**, 1090 (2010).

[14] I. Ginzburg, Multiple anisotropic collisions for advection-diffusion lattice Boltzmann schemes, Adv. Water Resour. **51**, 381 (2013).

[15] Z. Chai and T. S. Zhao, Lattice Boltzmann model for the convection-diffusion equation, Phys. Rev. E **87**, 063309 (2013).

[16] J. Wang, D. Wang, P. Lallemand, and L.-S. Luo, Lattice Boltzmann simulations of thermal convective flows in two dimensions, Comput. Math. Appl. **65**, 262 (2013).

[17] L. Li, R. Mei, and J. F. Klausner, Boundary conditions for thermal lattice Boltzmann equation method, J. Comput. Phys. **237**, 366 (2013).

[18] L. Li, R. Mei, and J. F. Klausner, Heat transfer evaluation on curved boundaries in thermal lattice Boltzmann equation method, ASME J. Heat Transfer **136**, 012403 (2014).

[19] L. Li, R. Mei, and J. F. Klausner, Multiple-relaxation-time lattice Boltzmann model for the axisymmetric convection diffusion equation, Int. J. Heat Mass Transfer **67**, 338 (2013).

[20] L. Li, C. Chen, R. Mei, and J. F. Klausner, Conjugate heat and mass transfer in the lattice Boltzmann equation method, Phys. Rev. E **89**, 043308 (2014).

[21] H. Yoshida, T. Kobayashi, H. Hayashi, T. Kinjo, H. Washizu, and K. Fukuzawa, Boundary condition at a two-phase interface in the lattice Boltzmann method for the convection-diffusion equation, Phys. Rev. E **90**, 013303 (2014).

[22] H. W. Liepmann and A. Roshko, *Elements of Gasdynamics* (Dover, New York, 2002).

[23] P. L. Mills, S. S. Lai, and M. P. Dudukovic, Solution methods for problems with discontinuous boundary conditions in heat

conduction and diffusion with reaction, Ind. Eng. Chem. Fund. **24**, 64 (1985).
[24] L. Li, R. Mei, J. F. Klausner, and D. W. Hahn, Heat transfer between colliding surfaces and particles, ASME J. Heat Transfer **134**, 011301 (2012).
[25] M. Kaviany, Heat transfer during impact, Encycl. Thermal Stresses 2188 (2014).
[26] L. G. Olson, G. C. Georgiou, and W.W. Schultz, An efficient finite element method for treating singularities in Laplace's equation, J. Comput. Phys. **96**, 391 (1991).
[27] Z. C. Li and T. T. Lu, Singularities and treatments of elliptic boundary value problems, Math. Comput. Model. **31**, 97 (2000).
[28] J.-S. Chen, C. Marodon, and H.-Y. Hu, Model order reduction for meshfree solution of Poisson singularity problems. Int. J. Numer. Meth. Eng. **102**, 1211 (2015).
[29] J. Wang, M. Wang, and Z. Li, A lattice Boltzmann algorithm for fluid-solid conjugate heat transfer, Int. J. Therm. Sci. **46**, 228 (2007).
[30] M. Wang, J. Wang, N. Pan, and S. Chen, Mesoscopic predictions of the effective thermal conductivity for microscale random porous media, Phys. Rev. E **75**, 036702 (2007).
[31] I. Ginzburg and D. d'Humières, Lattice Boltzmann and analytical modeling of flow processes in anisotropic and heterogeneous stratified aquifers, Adv. Water Res. **30**, 2202 (2007).
[32] I. Ginzburg, Lattice Boltzmann modeling with discontinuous collision components. Hydrodynamic and advection-diffusion equations, J. Stat. Phys. **126**, 157 (2007).
[33] K. Guo, L. Li, G. Xiao, N. AuYeung, and R. Mei, Lattice Boltzmann method for conjugate heat and mass transfer with interfacial jump conditions, Int. J. Heat Mass Transfer **88**, 306 (2015).
[34] D. d'Humières, Generalized lattice Boltzmann equations, Prog. Aeronaut. Astronaut. **159**, 450 (1992).
[35] I. Rasin, S. Succi, and W. Miller, A multi-relaxation lattice kinetic method for passive scalar diffusion, J. Comput. Phys. **206**, 453 (2005).
[36] D. d'Humières and I. Ginzburg, Viscosity independent numerical errors for lattice Boltzmann models: From recurrence equations to "magic" collision numbers, Comp. Math. Appl. **58**, 823 (2009).
[37] I. Ginzburg, Generic boundary conditions for lattice Boltzmann models and their application to advection and anisotropic-dispersion equations, Adv. Water Res. **28**, 1196 (2005).
[38] C. M. Bender and S. A. Orszag, *Advanced Mathematical Methods for Scientists and Engineers* (McGraw Hill, New York, 1978).
[39] I. Ginzburg and D. d'Humières, Local second-order boundary method for lattice Boltzmann model, J. Stat. Phys. **84**, 927 (1996).
[40] I. Ginzburg, F. Verhaeghe, and D. d'Humières, Study of simple hydrodynamic solutions with the two-relaxation-times lattice Boltzmann scheme, Commun. Comput. Phys. **3**, 519 (2008).